The Role of Interfacial Structure in The Evolution of Precipitate Morphology

by

Gang Chen

Dissertation submitted to the faculty of the

Virginia Polytechnic Institute and State University

in partial fulfillment of the requirements for the degree of

DOCTOR OF PHILOSOPHY

in

Materials Engineering Science

APPROVED:

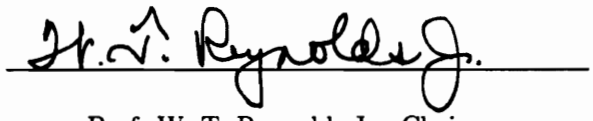

Prof. W. T. Reynolds Jr., Chairman

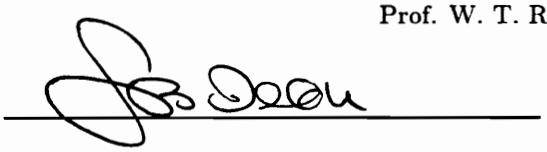

Prof. S. B. Desu

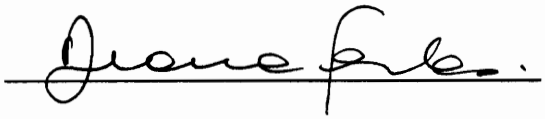

Prof. D. Farkas

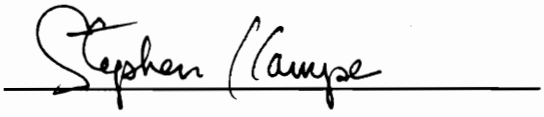

Prof. S. L. Kampe

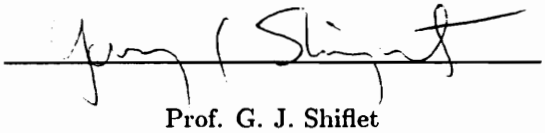

Prof. G. J. Shiflet

May, 1994

Blacksburg, Virginia

The Role of Interfacial Structure in The Evolution of Precipitate Morphology

by

Gang Chen

Committee Chairman: Prof. W. T. Reynolds Jr.

Department of Materials Science and Engineering

(ABSTRACT)

Three aspects of precipitate growth by a ledge mechanism in a Ni–45wt%Cr alloy were investigated. The strain energy for ledge formation and ledge growth kinetics and the emission of structural defects were studied experimentally during the growth of bcc laths from an fcc matrix.

The elastic strain energy of a growth ledge as a function of the ledge location was estimated using an Eshelby–type model. Ledge nucleation is only likely at facet areas where the interaction energy between the ledge and the precipitate is negative. Ledges form with the lowest strain energy on the broad habit plane of coherent precipitates. On a partially coherent lath the strain energy is lowest for a ledge located on the facet perpendicular to the crystallographic invariant line. This situation favors precipitate lengthening in the invariant line direction.

Experimental measurement of growth kinetics of the precipitate was made to examine the mechanistic relationship between precipitate growth kinetics and its morphology. TEM was employed to measure overall precipitate growth kinetics as function of time, crystallographic orientations and ledge density. Results show the precipitates widen and thicken by a ledge mechanism following parabolic growth laws. Morphology of precipitates during aging is closely related to the ledge density.

Several types of defect emission from partially coherent interphase boundary in the alloy were observed using conventional and *in situ* hot stage TEM techniques. Prismatic dislocation loops expand and glide off from the precipitate. Perfect $\frac{a}{2}\langle 110\rangle_{fcc}$ dislocations glide away from the broad habit plane. Stacking faults emanated from the broad face of the laths were observed during precipitate growth. These defects result in steps in the interface and appear to compensate misfit in the broad face of the lath.

ACKNOWLEDGEMENTS

I would like to express my sincere appreciation to my thesis advisor, Prof. W. T. Reynolds Jr., without whom this work could not have been accomplished. His unreserved support, constant encouragement and enthusiasm as both a teacher and a friend are largely responsible for the final content of this thesis.

Professors S. B. Desu, D. Farkas, S. L. Kampe and G. J. Shiflet are gratefully acknowledged for their careful review of the manuscript. Special thanks are due Dr. H. I. Aaronson for his stimulating discussions. My colleague and friend Mr. Jhewn-Kuang Chen is gratefully acknowledged for his valuable discussions on interfacial structures and tremendous help with computer operations. In addition, thanks are due: Dr. G. Spanos for his constructive suggestions on TEM work and substantial help with computer calculations using Enomoto's model; Profs. J. K. Lee and P. H. Leo for enlightening discussions on strain energy calculations; Prof. G. J. Shiflet for making the Ni-Cr alloy used in this investigation; Prof. J. M. Howe for assistance with high resolution TEM work; Prof. G. C. Weatherly for providing a copy of C. P. Luo's Ph.D. thesis; Mr. Harry Dudley and Mr. Steve McCartney for assistance with lab work and Ms. Jane Doran for help with administrative tasks. Prof. G. Q. Lu, Drs. Chien C. Chiu, Baoping He, Yinshi Liu, and Chen-Hsiung Peng are thanked for their friendship and encouragement. Financial support of the Department of Materials Science and Engineering of VPI and the National Science Foundation are gratefully acknowledged.

I also would like to thank Southwest Jiaotong University and Prof. S. K. Liu for encouraging me to continue my education at VPI.

Finally, I would like to thank my family (in China) for their love and support. Particular appreciation is given to my wife Yujie and son Roger for their love, patience, understanding and encouragement during this study. I would like to dedicate this thesis to my parents.

TABLE OF CONTENTS

CONTENTS

LIST OF FIGURES

LIST OF TABLES

Chapter 1
INTRODUCTION

This work was initiated to investigate the mechanistic relationship between precipitate growth kinetics and its morphology. The morphology of precipitate produced by solid state transformations is one of the important parameters that affect a material's properties. The atomic mechanisms for migration of the interphase boundary of faceted precipitate have recently drawn a lot attention. When the precipitate and matrix phases differ in crystal structure and in composition, the interphase boundary between them generally migrates by a ledge mechanism[1, 2]. The lateral movement of ledges at the interface leads to advance of the precipitate perpendicular to its interphase boundary, i. e. precipitate growth[1, 3]. Therefore, the precipitate growth kinetics can be directly related to the geometric character of the ledges, such as ledge formation rate and ledge migration velocity[3, 4]. Several studies have shown that these parameters usually vary from system to system and implied they are also orientation–dependent[5]. In terms of classical nucleation theory, the formation of new ledges depends upon chemical supersaturation, interfacial energy, and strain energy[3, 6, 7, 8]. The migration kinetics of ledges are believed to be controlled by the kinetics of solute diffusion[2]. Several studies suggest that precipitate growth shape essentially depends upon the boundary orientation–dependence of precipitate growth kinetics[4, 9, 10, 11, 12, 13, 14, 15, 16, 17] or upon the anisotropic boundary mobility[1, 2]. Although the theories have achieved considerable success in predicting growth direction of precipitates, no explicit consideration and direct evidence of the mechanism of the precipitate reaction have been made. Knowledge of the boundary orientation dependence of the ledge growth kinetics is thus central to understanding the evolution of precipitate shapes. This study is intended to quantify effects of strain energy, ledge geometric features, and ledge migration rates on

different interphase boundaries during growth of precipitate laths in a Ni–45wt%Cr alloy.

The second chapter focuses on effects of strain energy on the formation rate of growth ledges in different boundary facets of the laths. The elastic strain energy for ledge formation at different locations on a lath–shaped precipitate was calculated for three different facets. A comparison of the minimum strain energy site for ledge formation calculated with experimental observation is offered as additional evidence in support of the earlier conclusion that precipitate grows in the direction of the minimum strain energy, i.e. the invariant line direction[16, 17]. The calculation for two types of interphase boundary, the coherent and partially coherent, were carried out. Thickening, widening and lengthening of precipitates are discussed to review the various ways ledge formation rates on three facets can influence precipitate shape growth.

The question of whether or not the precipitate ledge growth is a diffusion–controlled phenomenon is addressed in Chapter 3. Quantitative TEM was employed to measure overall precipitate growth kinetics as a function of time, and boundary orientation and related to the ledge growth mechanism. In a series of papers published in 1970's, Aaronson et al[18, 19, 20] reported that the average thickening kinetics of ferrite in Fe–C alloys were highly erratic and exhibited multiple kinetics, and that overall rates of lengthening and thickening of γ plates in a Al–15wt%Ag[21] were concluded to be interface controlled. In the present investigation, a comparison of several growth models with experimental results was made to test the generality of the earlier worker's findings. Geometric features of growth ledges on two facets were examined using conventional TEM and hot–stage TEM to determine the effective mobility of growth ledges, and the boundaries that contain them.

The fourth chapter presents evidence for how misfit compensating defects are emitted from the boundary between the precipitate and its matrix. This information is important for understanding how partial coherency is maintained at moving interphase boundaries.

Each chapter is essentially self-contained and includes its own introduction, results, discussion, and conclusions or summary. Reference to results or conclusions from other chapters is usually made to the published paper rather than to the chapter number. Cross–

referencing is greatly facilitated by noting that:

reference [22] is chapter 2.

Chapter 2

THE ELASTIC STRAIN ENERGY OF GROWTH LEDGES ON COHERENT AND PARTIALLY COHERENT PRECIPITATES

2.1 Abstract

The formation rate of growth ledges on a faceted precipitate strongly affects the growth kinetics and the shape of the precipitate. An Eshelby-type model is used to compare the strain energy associated with the nucleation of a ledge on different facet planes of a bcc precipitate in an fcc matrix. Ledge nucleation is only likely at facet areas where the interaction energy between the ledge and the precipitate is negative. The strain energy for ledge formation is not symmetric on any of the facet planes, but it is symmetric about the center of the precipitate. For coherent precipitates comparable to those observed in the Ni–Cr system, ledges form with the lowest strain energy on the broad facet or habit plane of the precipitate implying that precipitate thickening should occur faster than lengthening and widening. A procedure for modifying the Eshelby model is suggested to allow strain energy calculations of partially coherent precipitates. The strain energy for ledge formation on at least one type of partially coherent lath is lowest for a ledge located on the facet perpendicular to the crystallographic invariant line. This situation favors precipitate lengthening in the invariant line direction.

2.2 Introduction

Precipitate morphology can influence the properties of many types of alloys. The toughness of Fe–, Al– or Ti–based alloys, for example, depend to varying degrees upon whether

the precipitate phase is plate-shaped or equiaxed. It is, however, difficult to predict precipitate shapes *a priori*. Precipitates do not necessarily adopt an equilibrium shape, and kinetic considerations are often important.

Several approaches to predicting growth shapes have been proposed when the precipitate does not assume the equilibrium morphology. Bywater and Dyson suggested that in the case of needle-shaped precipitates, growth occurs in the direction of minimum interatomic mismatch between the precipitate and parent crystal lattices[9]. It was argued that this direction minimizes the strain energy density during growth. Using elements of the crystallographic theory of the martensite reaction, Dahmen and coworkers[10, 11, 14, 13] expanded this concept into the invariant line hypothesis. According to this theory, precipitates grow along a crystallographic invariant line, a direction of zero misfit determined by a transformation strain and a lattice rotation. The transformation strain and lattice rotation are obtained from a chosen lattice correspondence between the parent and product phases. The invariant line hypothesis has achieved considerable success predicting both the growth direction of precipitates and the orientation relationships between the matrix and precipitate[11, 12, 15, 16, 17].

On a related approach, the shape and habit plane of a coherent precipitate are predicted by minimizing the strain energy of the precipitate[23]. Khachaturyan suggests a growing precipitate selects a habit plane so as to minimize strain energy. Although this approach, like the invariant line theory, employs a transformation strain specified by a lattice correspondence, the habit plane is selected by minimizing an explicit expression for strain energy rather than by finding a good match between the precipitate and matrix lattices.

A third approach to predicting precipitate shape emphasizes the mobility of the boundary between the precipitate and matrix phases[1, 2]. The precipitate shape is taken to depend upon the anisotropy of boundary mobility. Boundary orientations with a higher mobility "grow out" leaving behind a precipitate enclosed by low mobility boundaries[1, 2]. The boundary mobility, in turn, is determined by the migration mechanism of the boundary. When the precipitate and matrix phases differ in crystal structure and composition,

the interphase boundary between them is generally coherent or partially coherent and migrates by a ledge mechanism[2]. The boundary advances through the lateral movement of growth ledges, or steps, in the boundary. Precipitate growth by a ledge mechanism has been confirmed repeatedly in a number of alloys[1, 24, 25, 26, 27].

The overall migration rate of a ledged boundary depends upon two factors: the ledge height and the frequency with which ledges sweep across the boundary[4, 3]. This frequency is a function of the lateral velocity of individual ledges and the formation rate of new ledges. The anisotropic boundary mobility theory for precipitate morphology implies that precipitate shape depends upon the boundary orientation-dependence of ledge formation and migration kinetics[1]. Boundary orientations with the highest product of the ledge height and the passage frequency will migrate with the greatest overall velocity. For precipitate growth over distances that are large compared to the ledge height, the passage frequency can be approximated simply by the ledge formation rate[4, 3].

If one assumes growth begins from a coherent precipitate nucleus enclosed by zero mobility boundaries, predicting precipitate shape from a mechanistic standpoint becomes a problem of predicting the habit planes on which ledge formation occurs most slowly[29]. A number of mechanisms for the formation of growth ledges have been identified[5, 30, 31, 7], but for the purposes of comparing ledge formation rates on faceted precipitates it is convenient to use a classical nucleation approach[3]. The nucleation rate of ledges on a particular habit plane is thus inversely proportional to the exponential of the free energy of formation of a critical ledge nucleus. The free energy associated with the formation of a faceted ledge nucleus is described by an expression of the form[3, 7, 32]:

$$\Delta G_{nucl} = V\Delta G_v + \Sigma A_i\gamma_i + E_{self} + E_{int} \tag{2.1}$$

where ΔG_v is the local volume free energy change during ledge formation at the nucleation

[1] This approach assumes the boundaries of a faceted precipitate each migrate by independent sets of ledges. Alternatively, the boundaries may grow by a single ledge system if the precipitate facet planes correspond to the orientations of the terrace, riser and kink planes of the growth ledges[28]. Whether growth occurs through the migration of single or multiple sets of ledges has not been determined for fcc/bcc crystal pairs.

site, V is the volume of the ledge nucleus, γ_i is the interfacial free energy of the i-th facet of the ledge riser and A_i is the area of this facet. E_{self} is the self-strain energy associated with the formation of an isolated ledge nucleus, and the last term, E_{int}, is the interaction energy arising from the superposition of the strain fields of the ledge nucleus and the precipitate[7]. The activation energy for ledge formation can be obtained by finding the extremum of this expression with respect to the shape and size of the ledge nucleus. This requires a γ-plot of the interphase boundary energy as well as detailed information about the strain field and concentration field around the ledge nucleus[33]. Unfortunately, little if any of this data is available, so a realistic calculation of the nucleus shape is not possible.

However, because previous work indicates that strain energy plays an important role in determining the location of ledge nucleation[32, 33, 34], the present study investigates how the strain energy for ledge formation changes with the location of the ledge nucleus on the precipitate. The contributions of interfacial energy and solute supersaturation to ledge formation are neglected for simplicity. The precipitate is assumed to have a faceted, lath shape (a rectangular parallelepiped), and the strain energy for ledge formation is calculated for various locations of the ledge. The calculation is carried out using an Eshelby misfitting inclusion model assuming a homogeneous, isotropic, and linear elastic medium. Parameters for the model are chosen to represent precipitation of a body-centered cubic (bcc) precipitate from a face-centered cubic (fcc) matrix in the Ni–Cr system. The coordinate system is chosen to reflect the relationship between the orientation of the precipitate lath and the crystallographic invariant line. The strain energy for ledge formation on a coherent precipitate and on a partially coherent precipitate with several different configurations of misfit dislocations are compared, and the effects of precipitate growth upon the ledge strain energy are explored.

2.3 Procedure

The strain energy associated with the formation of a ledge nucleus is calculated as a function of the location of the ledge using Eshelby's continuum elasticity theory[35]. The ledge nucleus and the precipitate on which it forms are treated as two isotropic, elastically interacting inclusions with the same elastic constants. The strain energy accompanying the formation of a ledge nucleus E_{total} is expressed as the sum of two components[35]:

$$E_{total} = E_{self} + E_{int} \tag{2.2}$$

E_{self} represents the self-elastic strain energy associated with the formation of the ledge nucleus in the absence of the precipitate particle on which it forms, and E_{int} is the interaction energy between the strain fields of the ledge nucleus and the precipitate. The self-strain energy is calculated from an integral over the volume of the ledge, $V(I)$, [35]:

$$E_{self} = \frac{1}{2} \iiint_{V(I)} \left\{ e_{ij}^{T} - e_{ij}^{c}(\mathbf{r}) \right\} P_{ij}^{T} \, dV(\mathbf{r}) \tag{2.3}$$

The strain tensors, e_{ij}^{T} and e_{ij}^{c}, represent the stress-free transformation strain and the constrained strain, respectively, and $\mathbf{r}$ is a position vector originating from the center of the precipitate[2]. The stress-free transformation strain is the geometric strain the matrix phase undergoes to become the precipitate phase. The constrained strain is the actual strain that arises due to the restraining forces imposed on a precipitate by its surrounding matrix. P_{ij}^{T} is a hypothetical stress obtained through the assumption of linear elasticity: $P_{ij}^{T} = C_{ijkl} \, e_{kl}^{T}$. The elastic interaction energy between the ledge (denoted by I) and the precipitate (denoted by J) is given by integrals over the ledge volume and the precipitate volume[36]:

$$\begin{aligned} E_{int} \;=\; -\frac{1}{2} \Bigg\{ & \iiint_{V(I)} e_{ij}^{c}\,(J\!:\!\mathbf{r})\, P_{ij}^{T}(I)\, dV(\mathbf{r}) \\ & + \iiint_{V(J)} e_{ij}^{c}\,(I\!:\!\mathbf{r})\, P_{ij}^{T}(J)\, dV(\mathbf{r}) \Bigg\} \end{aligned} \tag{2.4}$$

[2]The usual tensor suffix notation is employed. A repeated suffix within a single term is to be summed over the orthogonal coordinate axes 1, 2 and 3, and a comma in a suffix indicates differentiation with respect to the trailing indices.

The geometry of the precipitate and the ledge nucleus enter the problem through the constrained strain. An analytical expression for e^c_{ij} has been derived for the case of rectangular parallelepiped-shaped inclusions by Lee and Johnson[37, 36]. Using their expression for the constrained strain around a faceted, rectangular-shaped precipitate and ledge nucleus, the constrained strain in Equations (2.3) and (2.4) can be written:

$$\begin{aligned} e^c_{ij} &= \frac{1}{8\pi(1-\nu)} \Big\{ e^T_{kl}\, \psi(\mathbf{r})_{,klij} - 2\nu\, e^T_{kk}\, \phi(\mathbf{r})_{,ij} \\ &\quad -2(1-\nu) \Big[e^T_{ik}\, \phi(\mathbf{r})_{,kj} + e^T_{jk}\, \phi(\mathbf{r})_{,ki} \Big] \Big\} \end{aligned} \tag{2.5}$$

where $\phi(\mathbf{r})$ and $\psi(\mathbf{r})$ are the ordinary harmonic potential and the biharmonic potential functions[38]. The functions $\phi(\mathbf{r})$ and $\psi(\mathbf{r})$ are defined by the integrals:

$$\phi(\mathbf{r}) = \iiint_V \frac{1}{|\mathbf{r}-\mathbf{r}'|} dV(\mathbf{r}') \tag{2.6}$$

and

$$\psi(\mathbf{r}) = \iiint_V |\mathbf{r}-\mathbf{r}'| dV(\mathbf{r}') \tag{2.7}$$

Inspection of Equations 2.3–2.5 indicates the strain energy for ledge formation is intimately related to the stress-free transformation strain. This is a system dependent quantity related to the crystal structures, lattice parameters, and the lattice correspondence between the matrix and precipitate phases.

For the present investigation, parameters appropriate to the precipitation of Cr-rich laths in Ni-rich binary Ni–Cr alloys were employed. This system was chosen because of the availability of detailed crystallographic and interfacial structure data on the precipitation process[16, 17, 39]. In addition, the laths closely resemble a rectangular parallelepiped. Figure 2.1 a shows the morphology of the precipitates formed in a Ni–45 wt% Cr alloy, and Figure 2.1 b shows the shape and orientation of the model precipitate employed in these calculations.

The matrix phase is the Ni-rich, face-centered cubic solid solution and the precipitate is the Cr-rich, body-centered cubic phase. The average aspect ratio of precipitates formed

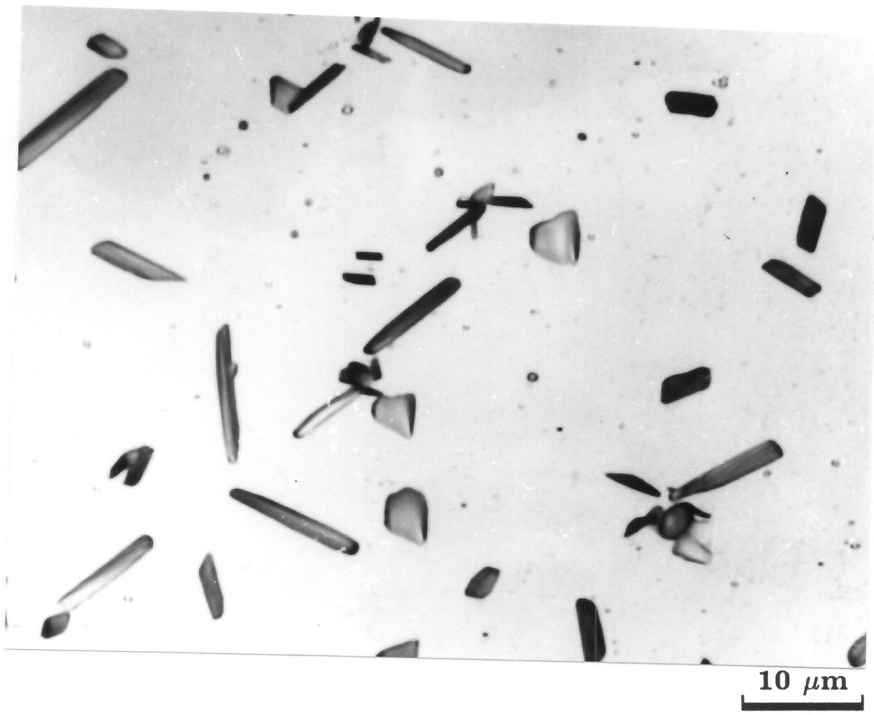

(a)

Figure 2.1: (a) Optical micrograph of bcc precipitates formed from fcc solid solution; Ni–45 wt% Cr solution treated at 1300°C for 10,800 s, quenched in ice brine, and aged at 1050°C for 36,000 s. (b) Shape and orientation of the precipitate and ledge nucleus employed in the calculation. The 1-axis is 5.19° from $[111]_{fcc}$, the 2-axis is the invariant line, 5.19° from $[\bar{1}01]_{fcc}$, and the 3-axis $[1\bar{2}1]$ is normal to the broad facet.

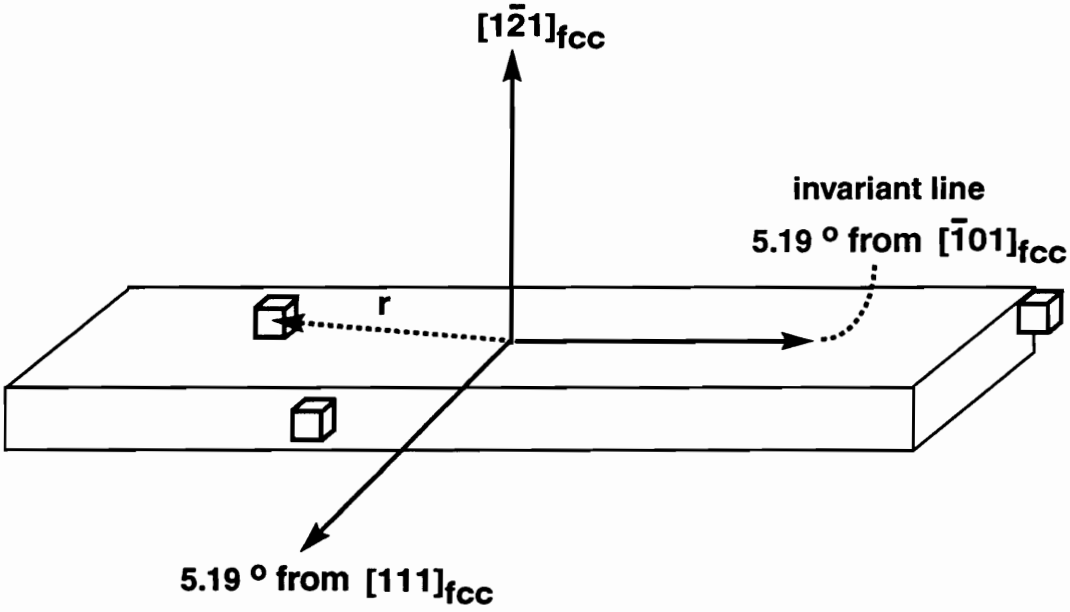

(b)

Figure 2.1, cont.

by quenching the fcc phase from 1300°C to room temperature and then aging the supersaturated solid solution for 10 hours at 1050°C is 1 : 5 : 17.5 [17]. The dimensions of the precipitate employed in the calculations is $10nm \times 50nm \times 175nm$, the approximate size at which these precipitates lose coherency[17]. The ledge nucleus is arbitrarily chosen to be a cube $0.448nm$ on a side, roughly the height of one fcc unit cell on the precipitate habit plane.

Luo and Weatherly have shown that the habit plane or broad facet of the bcc laths in this system is $(1\ \bar{2}\ 1)_{fcc}$, the long side facet of the precipitates is close to $(1\ 1\ 1)_{fcc}$ and the precipitate and matrix are in a Kurdjumov-Sachs (KS) orientation relationship[16, 17]. In this work, the habit plane $(1\ \bar{2}\ 1)_{fcc}$ and the KS orientation relationship were used to calculate an *approximately* invariant line of $[\overline{1.16045}\ \overline{0.080225}\ 1]_{fcc}$, a direction approximately 5.19° from $[\bar{1}\ 0\ 1]_{fcc}$. The IL direction lies in the broad facet and is parallel to the long axis of the lath. Details of how the approximate IL was determined and how the stress-free transformation strain was obtained from the transformation displacements are included in the Appendix. The three orthogonal coordinate axes chosen for the strain energy calculations (Figure 2.1 b) include the approximate invariant line, the normal to the broad facet (the $[1\ \bar{2}\ 1]_{fcc}$ direction), and the the cross product of the first two axes (i.e., $[1.91977\ 2.16045\ 2.40000]_{fcc}$, a direction about 5.19° from $[111]_{fcc}$). The stress-free transformation strain in the chosen coordinate system determined from the displacement tensor, $u^T_{i,j}$, is:

$$e^T_{ij} = \frac{1}{2}\left(u^T_{i,j} + u^T_{j,i}\right) = \begin{pmatrix} -0.0305166 & -0.1323397 & -0.1082530 \\ -0.1323397 & 0.0000182 & -0.0844203 \\ -0.1082530 & -0.0844203 & 0.0446893 \end{pmatrix} \tag{2.8}$$

where the vector **u** describes the displacements the fcc lattice undergoes to transform to the bcc lattice.

The strain energy for the formation of a ledge nucleus as a function of the location of the nucleus on the precipitate lath was calculated using Equations 2.2 through 2.5 and the elastic constants $C_{11} = 2.4686 \times 10^{11}\mathrm{N/m^2}$, $C_{12} = 1.5234 \times 10^{11}\mathrm{N/m^2}$ [40], and $\nu =$

$\frac{C_{12}}{C_{11}+C_{12}} = 0.3816$ [41]. Since nine components of e_{ij}^T are nonzero, Equation 2.5 has numerous terms and is tedious to calculate. Consequently, expressions for the constrained strain were generated by computer using a symbolic manipulator (Mathematica). These expressions were tested for accuracy by partitioning a single precipitate into several parts and assuring the strain energy obtained via Equation (2.2) was the same as the self-energy of the whole precipitate.

The method employed here to calculate strain energy assumes the precipitate and the matrix are coherent with each other. However, the laths under consideration are known to become partially coherent once they grow beyond a critical size[16, 17]. Consequently, the strain energy for ledge formation was calculated for a fully coherent precipitate, and for a simulated partially coherent precipitate as well.

The partially coherent precipitate is simulated by allowing normal stresses to be transmitted across the interphase boundary but not shear stresses. It is assumed arrays of dislocations in a partially coherent boundary relieve elastic misfit in the direction of the dislocation's Burgers vectors. Thus, rather than eliminate all the elastic shear stress across the interphase boundary, an array of misfit dislocations is taken to eliminate the elastic shear stress in a single direction. Elastic interactions between misfit dislocations and the nucleating ledge are neglected.

Three different arrangements of misfit dislocations are considered. Each arrangement, shown schematically in Figure 2.2, consists of one or more arrays of dislocation loops encircling the precipitate lath. Relaxation of the misfit strain by an array of misfit dislocations is incorporated into the calculation by modifying the displacement tensor. A sufficient supply of misfit dislocations is envisioned to be present so that the shear component of the displacement tensor $u_{i,j}^T$ in the direction of the dislocation Burgers vector can be set equal to zero. The strain energy for the ledge is then calculated with the modified stress-free transformation strains shown in Figures 2.2 a, b and c in the same manner as for a coherent precipitate.

In a crystallographic sense, changing the transformation strain alters the correspondence

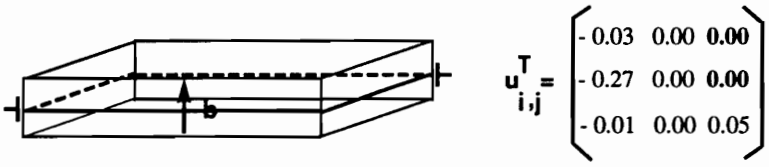

(a)

Figure 2.2: Schematic illustrations of three types of dislocation arrays enclosing a partially coherent precipitate lath and the corresponding stress-free transformation strains. (a) Orientation of the 12 loop dislocation loops — edge type misfit dislocations loop the precipitate and lie in the long facet and in the short facet, (b) orientation of the 23 dislocation loops — edge type misfit dislocations loop the precipitate and lie in the broad facet and in the short facet, (c) orientation of the network dislocations — a combination of 12 dislocations loops 12 and 23 dislocations loops.

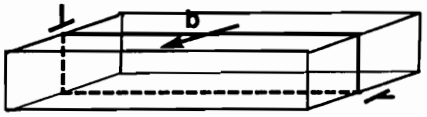

$$u^T_{i,j} = \begin{pmatrix} -0.03 & 0.00 & -0.21 \\ \mathbf{0.00} & 0.00 & -0.17 \\ \mathbf{0.00} & 0.00 & 0.05 \end{pmatrix}$$

(b)

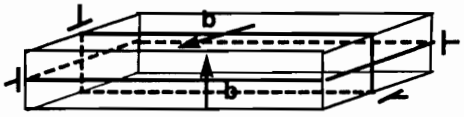

$$u^T_{i,j} = \begin{pmatrix} -0.03 & 0.00 & \mathbf{0.00} \\ \mathbf{0.00} & 0.00 & \mathbf{0.00} \\ \mathbf{0.00} & 0.00 & 0.05 \end{pmatrix}$$

(c)

Figure 2.2, cont.

between the parent and product crystal lattices. However, the modified transformation strain is only used as an expedient in the strain energy calculation. The orientation relationship between the precipitate and the matrix is left unchanged. This apparent dichotomy is acceptable during a precipitation reaction because the transformation mechanism is diffusional rather than displacive. There is no atomic correspondence between the precipitate and the parent matrix phases, so the deformations occurring at the transformation interface do not necessarily represent the purely operational deformation of the stress free transformation strain. The altered transformation strain employed for partially coherent precipitates can be viewed as the sum of two component strains: one representing the conventional stress-free transformation strain and a second resulting from the slip at the interphase boundary that takes place when the precipitate loses coherency.

There are many misfit dislocation arrays that could conceivably appear during the loss of precipitate coherency. The character of the dislocation arrays in Figure 2.2 were chosen to be consistent with defects observed by Luo and Weatherly[16]. Interfacial dislocations were observed by these workers to lie parallel to the invariant line in the long, narrow facet (henceforth, the long facet) with a Burgers vector of the $\frac{a}{3} < 1\ \bar{1}\ 1 >_{fcc}$ type[17]. Figure 2.2 a schematically represents the orientation of an array of dislocation loops, referred to as the 1–2 loop, that surrounds the long facet and the short end facet (the facet perpendicular to the IL). Figure 2.2 b describes the orientation of an array of dislocation loops which surrounds the short, end facet and the broad facet (the 2–3 loop). The Burgers vectors for the dislocation loops are indicated by arrows; they are assumed to lie in the interface plane so as to provide maximum misfit compensation in both cases. The array represented by Figure 2.2 c is the network dislocation array and is a combination of the 1–2 loop and the 2–3 loop. For the case of the 1–2 loop, the $u^T_{i,3}(i \neq 3)$ components are zero, and for the 2–3 loop, $u^T_{i,1}(i \neq 1)$ vanish. All components $u^T_{i,3}(i \neq 3)$ and $u^T_{i,1}(i \neq 1)$ are zero for the dislocation network case.

2.4 Results and Discussion

2.4.1 Coherent Precipitate

Nucleation of a ledge is the initial stage in the advance of a facet during growth. Although the interphase boundary energies are important factors in Equation (2.1), it was found that the strain energy terms made ledge formation effectively impossible at some locations on the precipitate facet planes. This conclusion was also reached in a study of ledge formation during precipitate coarsening[6]. Thus, comparison of the strain energy required to form a ledge at various locations should provide a reasonable indication of where growth ledges can be expected to nucleate and which of the facets can be expected to grow with the greatest kinetics.

One might expect that the facet with the smallest components of the stress-free transformation strain would be the one with the lowest strain energy and the largest ledge nucleation kinetics. However, the strain energy for ledge formation depends upon the constrained strain as well as the stress-free transformation strain, and these two quantities can differ substantially. Figure 2.3 compares the components of the constrained strain at the center of a ledge forming at the middle of the short facet and at the center of a ledge forming at the middle of the broad facet. Both constrained strain tensors are significantly different from the corresponding components of the stress-free transformation strain. Although the stress-free transformation strains are quite large, the actual constrained strains are not so large as to violate the assumption of linear elasticity. Also, neither shear nor dilatational components of the constrained strain are zero along the invariant line direction. This indicates that for lath-shaped precipitates, unlike the case suggested for needle-shaped precipitates[9], lattice misfit in a single direction is not necessarily an accurate indicator of the actual strain surrounding a precipitate.

The strain energy accompanying ledge formation was calculated at 25 locations on each of the six facet planes. The relative ledge locations used for each of the facets are shown in Figure 2.4. The strain energy was then represented by a third order, least-squares

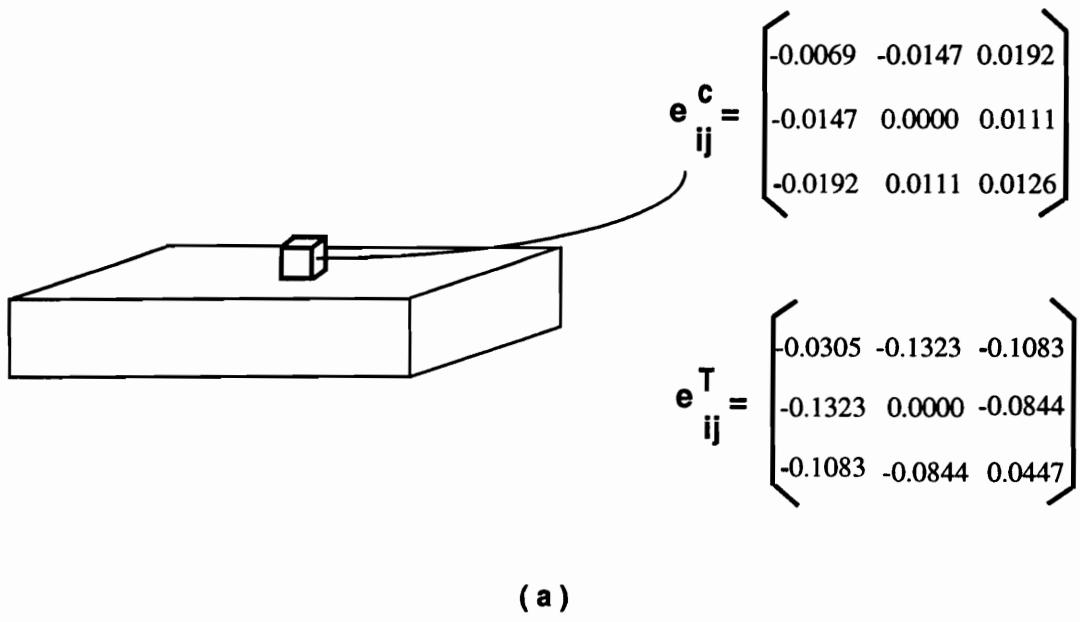

Figure 2.3: The constrained strain, e^c_{ij}, for a ledge located (a) at the center of the broad facet, and (b) at the center of the short facet.

polynomial fitted to the values calculated at the 25 ledge locations and displayed as a three dimensional surface plot and as a density plot. The strain energy plots for ledge formation on the broad facet of a coherent precipitate are shown in Figure 2.5. In the three dimensional representation (Figure 2.5 b), the strain energy for ledge formation is plotted as a normalized quantity along the vertical axis $\left(E_{norm} = \frac{E_{self}+E_{int}}{E_{self}}\right)$, and the two horizontal axes represent the edges of the facet plane. Figure 2.5 c presents the same information in a plot of isostrain energy contours in the facet plane.

The location dependence of the strain energy results from the interaction between the strain field of the ledge nucleus and the strain field of the precipitate. This component of the strain energy, E_{int}, varies with the position of the ledge nucleus on the facet plane and can be positive (inhibiting ledge formation) or negative (aiding ledge formation). When the normalized strain energy is zero, the interaction energy exactly cancels the ledge self-strain energy and there is no net strain contribution to the ledge formation energy. The relative magnitudes of the self-strain energy and the interaction strain energy depend upon the relative sizes of the ledge and the precipitate (see Equations 3 and 4). Since the size of the precipitate is much larger than that of the ledge, the interaction can exceed the self energy of the ledge. The self-strain energy for a cube-shaped ledge $0.448nm$ on a side is $1.3555 \times 10^{-18}J$ (using Equation 2.3). The chemical driving force for the formation of the same volume of the precipitate in this system is estimated using a subregular solution model and available thermodynamic data[42, 43] to be approximately $3.8235 \times 10^{-20}J$. Thus, it appears that the chemical driving force alone is not great enough to overcome the self-strain of the ledge, and if the ledge is to nucleate at all, it must do so at a location with a large negative interaction energy.

It can be seen by inspection of Figures 2.5 b and c that the normalized strain energy[3] for ledge formation has the largest and the smallest values when the ledge nucleates along an edge of the precipitate's broad facet. This indicates that the elastic interaction between

[3]The actual strain energy can be obtained by multiplying the normalized strain energy by the self-strain energy of the ledge, $1.36 \times 10^{-18}J$.

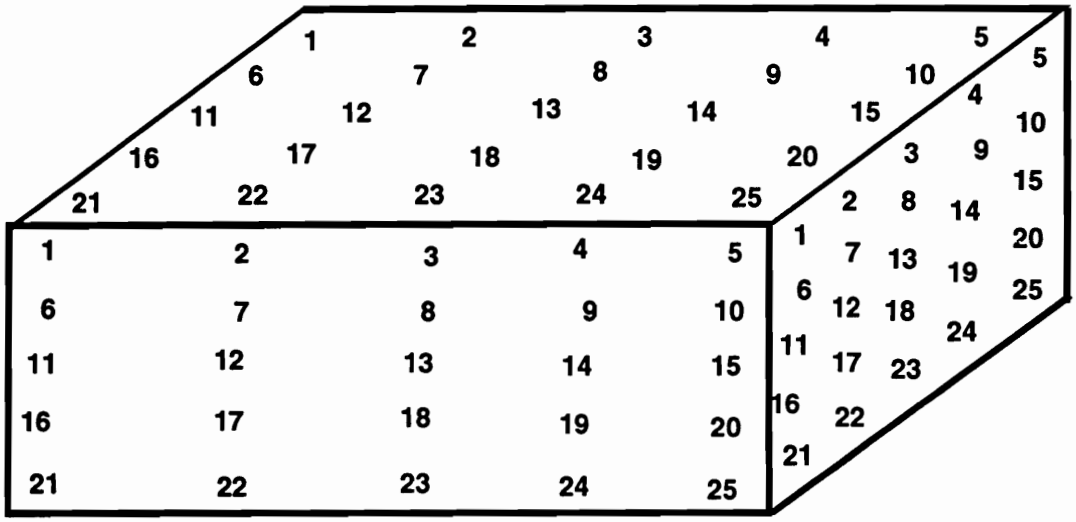

Figure 2.4: The 25 locations on each facet plane (the broad facet, the long facet and the short facet planes) at which the strain energy for ledge formation was calculated.

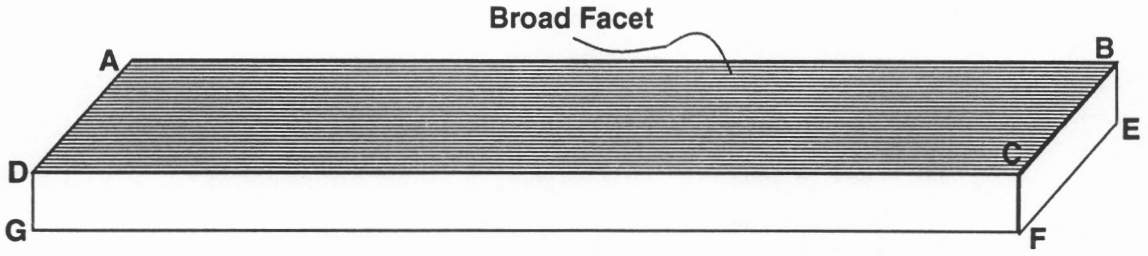

(a)

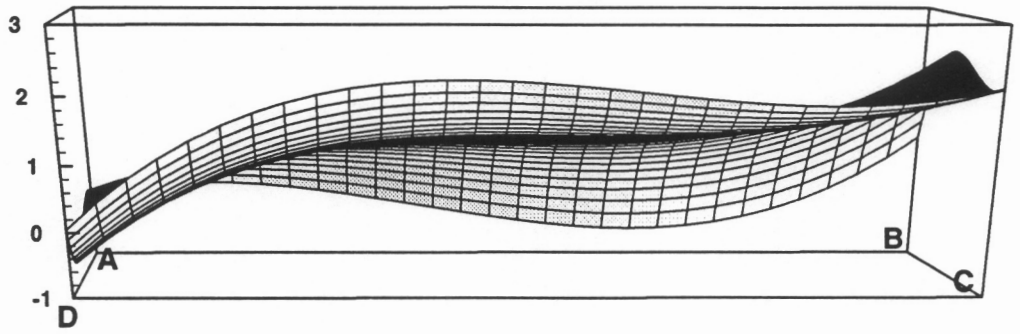

(b)

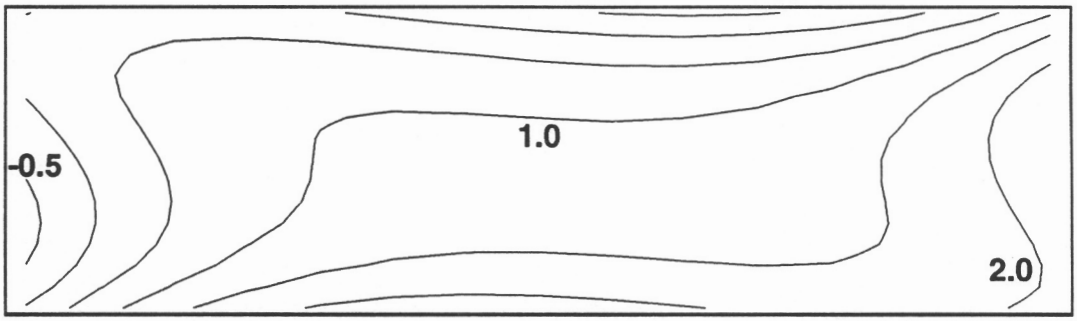

(c)

Figure 2.5: The strain energy distribution for ledge formation on the broad facet of a coherent precipitate. (a) the broad facet on the precipitate, (b) the normalized strain energy as a function of the location on the broad facet, and (c) a contour plot of b.

a ledge and the precipitate is greatest for ledges along the edges of the broad facet. Figures 2.6 b and c show similar results for ledge formation on the long facet and on the short facet. On the long facet, the minimum normalized strain energy is 0.0085 whereas the minimum normalized strain energy on the short facet (Figure 2.6 b) is -0.3621. The absolute minimum normalized strain energy for ledge formation is located on the broad facet and is -0.5277.

The normalized total strain energy is not symmetric on any given facet plane. However, the distribution of the strain energy on each pair of parallel facets was found to be symmetric about the center of the precipitate. That is, the value of the normalized strain energy at any point on a facet, (a, b, c), is the same at the point $(-a, -b, -c)$ on the opposite facet. Thus, there are two points that have the minimum strain energy for ledge formation. The locations of the minimum strain energy for ledge formation on the coherent precipitate are indicated in Figures 2.7.

The result that the minimum in the strain energies occur at opposite points on the facets is consistent with experimental observations by Luo and Weatherly[17] who found the two broad facets of the precipitate contain ledges that rotate the two interface planes in the same direction. This situation would occur if, as the strain energy calculation suggests, the ledges on opposing facets nucleate at diametrically opposed facet edges.

It is interesting to note that the normalized strain energy for ledge formation on the short facet of the coherent precipitate is always positive. This means that the interaction component of the strain energy is never negative enough to offset the self-strain energy of the ledge nucleus. Since ledge formation on this facet corresponds to lengthening of the precipitate in the invariant line direction, it appears that growth in this direction is not favored. If strain energy is an important component of the total energy for ledge formation, Figure 2.7 indicates ledges should form most readily on the broad facet and thickening of the precipitate should occur faster than lengthening or widening.

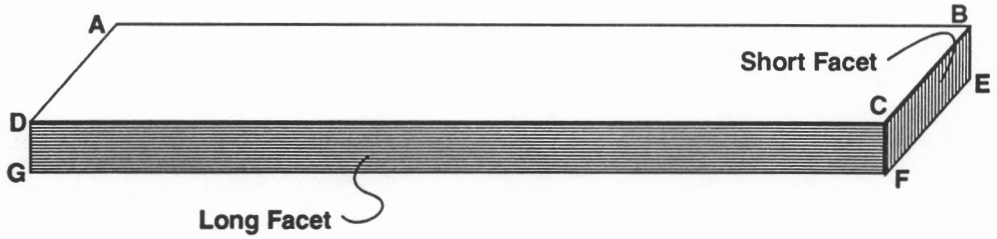

(a)

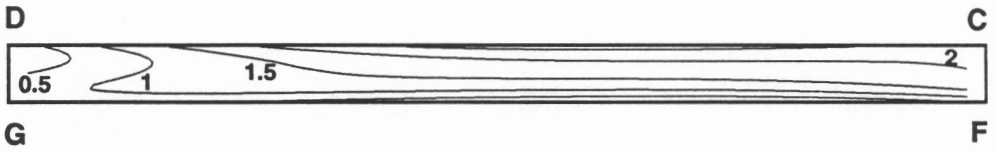

(b)

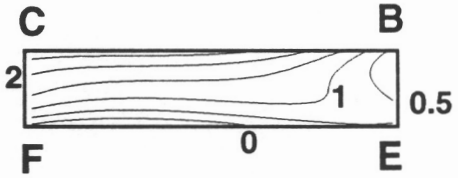

(c)

Figure 2.6: The strain energy distribution for ledge formation on the long facet and on the short facet. (a) the long and short facets, (b) contour plot of the normalized strain energy on the long facet, and (c) contour plot of the normalized strain energy on the short facet.

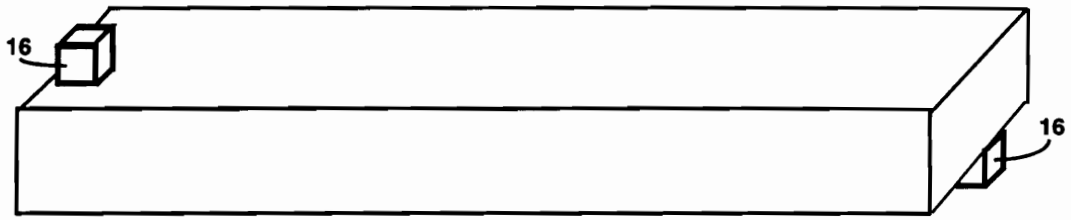

Figure 2.7: Location of the minimum strain energy for ledge formation on a coherent precipitate.

2.4.2 Partially Coherent Precipitate

If the bcc precipitates in Ni–Cr actually thickened faster than they lengthened as the results for the coherent precipitate suggest, the aspect ratio of the precipitates would drop with time. Since this does not seem to be born out by experiment, the minimum strain energy location must change when the precipitate loses coherency. The location of the minimum strain energy for ledge formation for each of the three types of dislocation arrays is shown in Figure 2.8.

For the 1–2 loop (Figure 2.8 a), the location of minimum strain is the same as for the coherent precipitate, but the magnitude of the normalized strain is much greater (0.2279 for the 1–2 loop vs −0.5277 for the coherent case). The minimum strain energy for ledge formation on a precipitate enclosed with the 2–3 loop dislocation array (Figure 2.8 b) is located at the corner of the short facet. The magnitude of this minimum is −0.9520, substantially less than the minimum on a coherent precipitate. For the misfit dislocation network, the location of the minimum strain energy for ledge formation is the center on the long facet, Figure 2.8 c. The normalized strain for this case is 0.2397, slightly greater than the value for the 1–2 loop and much greater than that for the coherent precipitate.

Since both the 1–2 loop and network configurations increase the minimum strain energy for ledge formation relative to the coherent precipitate, these misfit dislocation arrays are not likely to assist ledge formation. The 2–3 loop, However, does reduce the strain energy for ledge formation significantly, particularly on the short facet. In this case, the formation kinetics for ledges are expected to be greatest on the short facet, providing, of course, that the precipitate is able to acquire 2–3 type misfit dislocations. Precipitate lengthening in the invariant line direction should then take place with greater kinetics than thickening or widening[29].

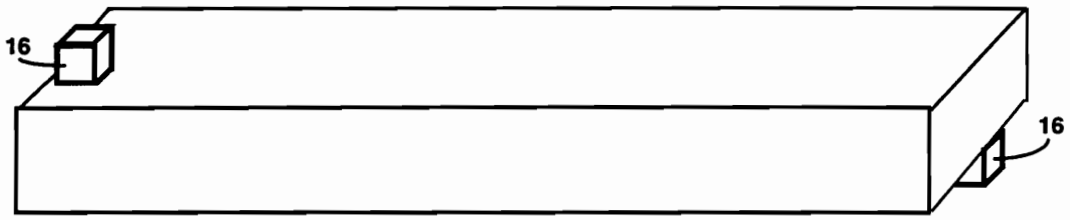

(a)

Figure 2.8: The location of the minimum strain energy for ledge formation on partially coherent laths (a) the 1–2 dislocation array at position 16 on the broad facet, (b) the 2–3 dislocation array at position 5 on the short facet, and (c) the network dislocation array at position 13 on the long facet.

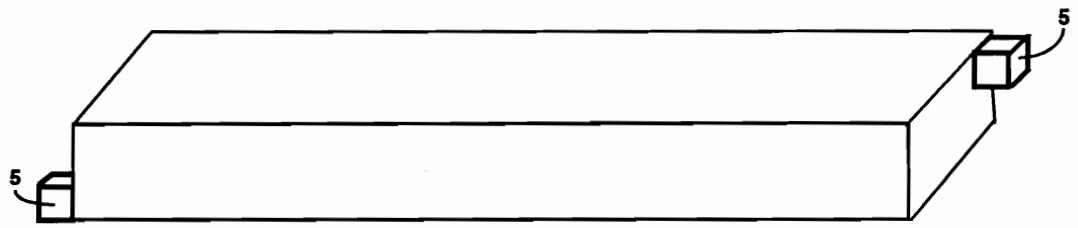

(b)

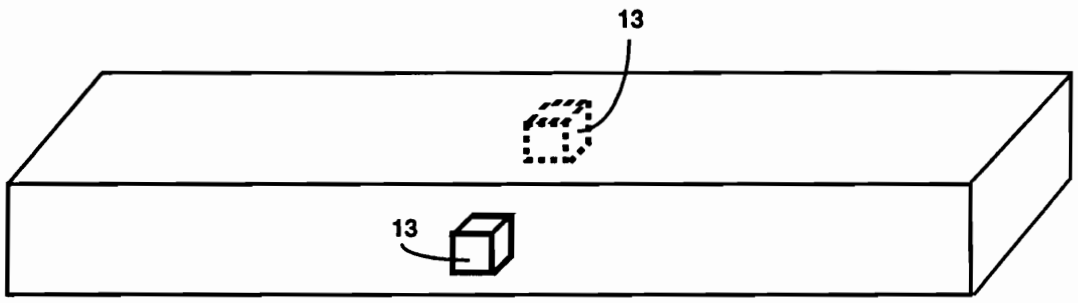

(c)

Figure 2.8, cont.

2.4.3 Effects of Precipitate Growth upon Ledge Formation Energy

If growth ledges form on the three facets with different rates, the migration rates of the facets will differ and the aspect ratio of the precipitate will change with time. To see how this affects the strain energy for ledge formation, the aspect ratio was altered to simulate growth in a direction normal to each of the three facet planes. Such growth corresponds to precipitate widening, lengthening, and thickening. These cases are represented schematically in Figure 2.9.

The three types of precipitate growth change the aspect ratio of the model precipitate used in the calculations in the following ways:

1. for widening, the aspect ratio is $a' : 17.5 : 1$ where $a' > 5$
2. for lengthening, the aspect ratio is $5 : b' : 1$ where $b' > 17.5$
3. for thickening, the aspect ratio is $5 : 17.5 : c'$ where $c' > 1$

Figure 2.10 shows how the minimum strain energy for ledge formation changes when the partial coherent precipitate (2–3 loop) lengthens, widens, or thickens. In Figure 2.10, the ledge is located on the short facet (position 5 in Figure 2.4). Although the three types of growth considered require ledge formation at locations other than the one with the lowest strain energy, the effect of aspect ratio is shown for ledge formation at a single location (the minimum strain energy site).

The strain energy for ledge formation changes with the aspect ratio of coherent and partially coherent precipitates. Some of this change is due to the increase in precipitate size. Because the strain field scales with precipitate volume, the interaction component of the ledge strain energy becomes greater (i.e., becomes more negative) with increasing precipitate size, and growth in any of the three directions increases the magnitude of the strain energy for ledge formation. Nevertheless, widening makes the ledge strain energy considerably more negative than thickening. Lengthening has little effect on the ledge formation energy. These trends are essentially the same for coherent and partially coherent

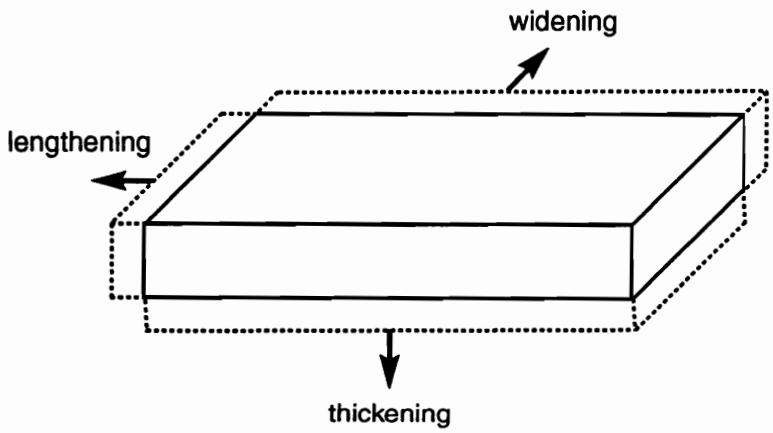

Figure 2.9: Schematic illustrations of three types of precipitate growth—thickening, widening, and lengthening.

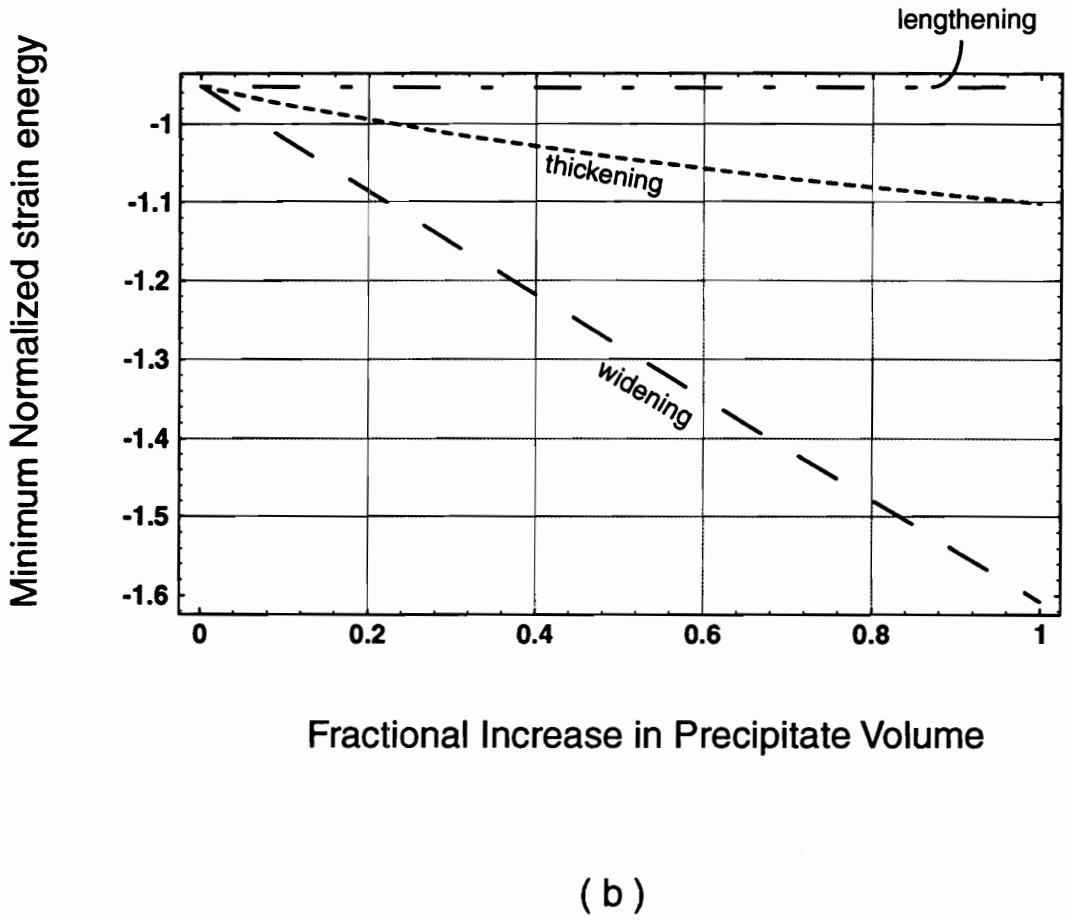

Figure 2.10: The variation in the minimum total strain energy for ledge formation with precipitate growth. Ledge formation on the short facet of a partially coherent precipitate (2–3 dislocation array).

precipitates, but the value of the minimum strain energy for ledge formation on the partially coherent precipitate is more negative than for the coherent precipitate.

A change in the aspect ratio could conceivably change the location of the most favorable site for ledge formation. This would occur during growth if the strain energy for ledge formation decreased more rapidly on one facet than on the others. To test this, the minimum strain energy site on each of the three facets of the partially coherent precipitate was determined during widening, lengthening and thickening. These results are represented in Figures 2.11 a, b and c, respectively. The three curves in each figure represent the lowest normalized strain energy for ledge formation on the long, short and broad facets. In comparing Figures 2.11 a-c, one can see that widening, lengthening and thickening generally decrease the strain energy for ledge formation, but the decrease occurs in parallel on the three facets. The most favorable site for ledge formation always remains on the short facet. Thus, the most likely site for ledge formation should not change during growth.

It should be noted that the changes in ledge formation energy with precipitate aspect ratio result from changes in the interaction energy between the ledge and the precipitate. Ledges are likely to form at the most favorable sites, and these sites are determined by the local strain field. This does not imply the precipitate will adopt the absolute minimum strain energy shape.

Finally, several limitations of the present approach should be noted. First, the Ni–Cr material used for the model parameters has a rather large anisotropy ratio, $\frac{2C_{44}}{C_{11}-C_{12}} \approx 2.8$ [40]. The use of isotropic elasticity undoubtedly results in some error, but the trends should not be affected greatly. Improvements will require the use of numerical methods such as those applied recently to calculate strain energies of misfitting precipitates[44]. In addition, no effort has been made to estimate the effect of interfacial energy nor the shape and size of the ledge nucleus on the ledge formation energy. These factors are probably important, but they are difficult to assess in a quantitative fashion given the present state of knowledge on the growth ledge formation process. The predictions of the present approach can be checked by experimentally determining the location of ledge formation and by identifying

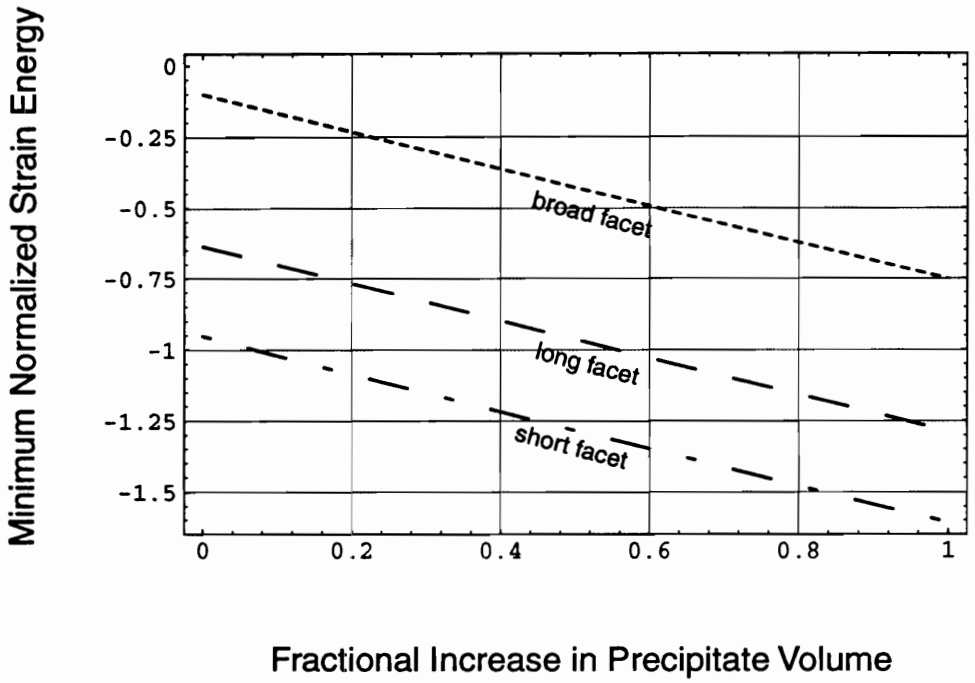

Figure 2.11: Comparison of the minimum strain energy for ledge formation on three facets of a partially coherent precipitate (2–3 dislocation array) with different processes of precipitate growth. (a) Precipitate widening, (b) Precipitate lengthening, (c) Precipitate thickening

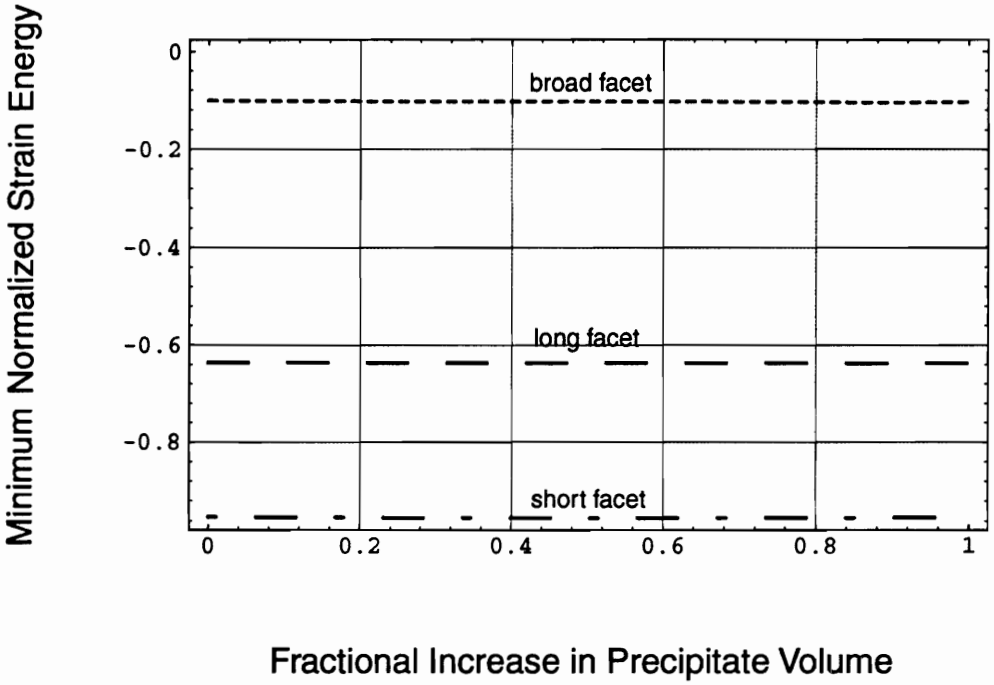

(b)

Figure 2.11, cont.

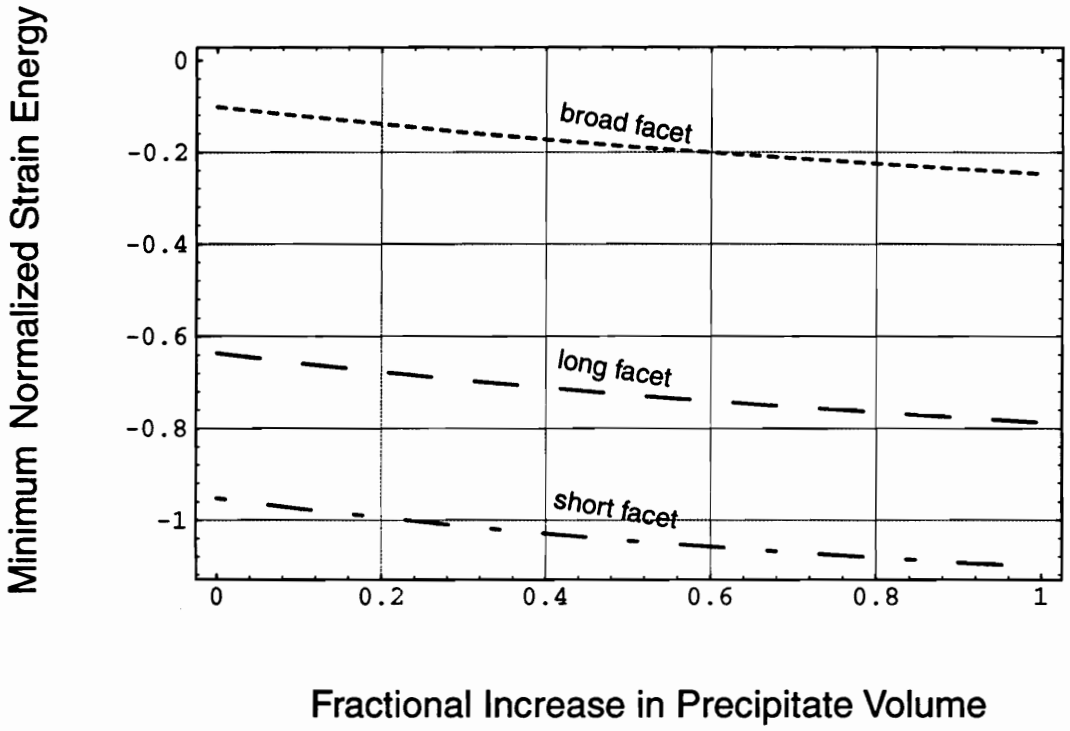

(c)

Figure 2.11 , cont.

the character of misfit dislocations in the precipitate facets.

2.5 Conclusions

The elastic strain energy for ledge formation on a lath-shaped precipitate in Ni–45%Cr was calculated using a method based upon Eshelby's classical work. The following are the principal conclusions obtained.

1. Although the components of the displacement tensor along the invariant line direction are zero, i.e. $u^T_{i'2} = 0$, the components of the constrained strain along this direction are not zero. As a consequence, there is substantial elastic strain energy associated with growth of a coherent lath in the invariant line direction.

2. The distribution of the elastic strain energy for ledge formation is not symmetric on any of the lath's facet planes, but it is symmetric about the center of the precipitate.

3. Ledge nucleation is only likely at facet areas where the ledge-precipitate interaction energy is negative. At other locations, the chemical driving force for ledge formation is probably not large enough to overcome the self-strain energy of the ledge.

4. Locations of the minimum and maximum elastic strain energy for ledge formation on the coherent precipitate are along the edges or the corners of the facet planes.

5. For a coherent precipitate, the location of the absolute minimum strain energy for ledge formation is at one end of the broad facet (habit) plane. Neglecting other contributions to the energy for ledge formation, this location favors precipitate thickening.

6. The effects upon the ledge strain energy of three types of misfit dislocation arrays were considered. Of these, a parallel array of dislocations looping the precipitate and lying in the broad facet and the short facet assists ledge formation the most.

7. The minimum strain energy site for ledge nucleation on the partially coherent precipitate is on the short facet. Lengthening of the lath in the invariant line direction is

favored over thickening and widening.

8. During ledgewise growth, the location of the lowest strain energy site for ledge formation does not change. Lengthening remains the favored growth direction for the partially coherent precipitate. Widening, and thickening to a lesser degree, make lengthening more favorable.

Chapter 3

EFFECTS OF GROWTH LEDGE DENSITY ON PRECIPITATE MORPHOLOGY IN A Ni–Cr ALLOY SYSTEM

3.1 Abstract

The effect of growth ledge formation kinetics on the evolution of precipitate morphology in a Ni–45wt%Cr alloy was investigated. The migration kinetics of two facets on intragranular laths were measured with TEM. Relatively short aging times were chosen to obtain the partially coherent and intragranular lath shape precipitates in order to measure growth kinetics. To understand the relationship between growth kinetics of precipitates and growth ledge on different interphase boundaries several microstructural parameters were measured as function of aging time. Experimental results show that widening and thickening kinetics of precipitates by the ledge mechanism follow parabolic growth laws. The morphology of precipitates during growth is closely related to the ledge heights, density and whether the ledge coalesce. The difference in overall growth rates of face 1[1] and face 3[2] is discussed in terms of ledge formation rates. Calculations using several theoretical growth models show a good agreement with experimental results.

3.2 Introduction

Ledges at interphase boundaries have been known to play an integral role in the growth of precipitates[1, 2, 3, 4, 8, 45]. In a general theory of precipitate morphology[1], Aaronson

[1]The present authors refer the side long face to the face 1, see[22]
[2]The present authors refer the broad face to the face 3, see[22]

first proposed that the shape of a precipitate during growth, which can differ significantly from the equilibrium shape, is a function of the relative mobilities of the boundaries enclosing the precipitate. It was suggested that a structural barrier to migration exists at partially coherent boundaries, so these boundaries move by a ledge-wise growth mechanism with reduced kinetics[1].

The role of ledges in the growth process has been investigated in several studies. The earliest direct measurement was made using thermionic emission electron microscopy[18, 19, 20]. This technique was used to monitor the *in situ* isothermal growth of ferrite plates on polished surfaces. Two types of ferrite growth behavior were discovered. The lengthening of ferrite plates in binary Fe–C alloys took place more or less smoothly[19], while the average thickening kinetics were highly erratic and exhibited multiple kinetics: linear, parabolic, stepped kinetics and combinations thereof[18]. A subsequent study of the thickening and lengthening of hcp γ plates in a Al–15wt%Ag alloy with hot–stage transmission electron microscopy[21] showed that thickening and lengthening of the plates was accomplished by the uniform advance of growth ledges. Although the ledge velocity was found to be that permitted by volume diffusion, overall rates of plate lengthening and thickening were concluded to be interface controlled.

A study of the influence of growth ledges on coarsening of γ' precipitates in Al–Ag[32] was made by Aikin and Plichta. During coarsening, changes in precipitate shape and size are driven by interfacial energy rather than by the chemical supersaturation that drives growth. These workers found that measured thickening rates of the plates are inversely proportional to the interledge spacing. In addition, the rate of ledge nucleation was inferred from the constant interledge spacing to be relatively constant. Consequently, the precipitate thickness increased linearly with the aging time. The change in plate diameter did not follow any discernible temporal law.

The predominant growth direction of precipitates can be predicted in many systems by the invariant line theory developed by Dahmen and his coworkers[10, 11, 12, 13]. This approach is also a useful tool for predicting orientation relationships and aspects of the

precipitate/matrix interfacial structure of many diffusional transformations. It has been found that precipitate rods and laths elongate in the invariant line direction and the broad faces of plates contain the invariant line. In terms of the general theory for precipitate morphology[1], this implies that the boundary perpendicular to the crystallographic invariant line direction must migrate with higher kinetics than boundaries that contain this direction. However, there is currently no clear connection between the ledge mechanism responsible for boundary migration and the crystallographic theory of invariant line model.

The present study was undertaken to relate the boundary migration mechanism with the crystallography of the precipitation process. A Ni–45wt%Cr alloy, in which Cr–rich bcc lath-shaped precipitates formed in a Ni–rich fcc matrix, is used for this purpose. The crystallography and interphase boundary structure of the precipitates in this alloy have been documented previously by Luo and Weatherly[16, 17, 39]. Growth ledge densities on two partially coherent boundaries of lath-shaped precipitates were made with TEM and related to the migration kinetics of the boundaries. Geometric characteristics of the ledges and their role in the growth process were also assessed. As a limiting case, the experimental migration kinetics of the facets are compared with theoretical models for diffusion-controlled migration of disordered boundaries.

3.3 Experimental Procedures

3.3.1 Sample preparation

Ingots of the Ni-45wt%Cr alloy were made by vacuum arc-melting appropriate amounts of 99.99% pure Ni and Cr. Sections $10 \times 10 \times 100$ mm in size were cut from approximately 400 g ingots, placed in quartz capsules and evacuated to a pressure of 10^{-5} torr. The capsules were back-filled twice with purified argon and evacuated to 10^{-5} torr before sealing and homogenizing for 48 hours at 1320°C. Homogenized material was cold-rolled to 0.5 mm thickness sheet, solutionized in vacua at 1300° C for 4 hours and quenched in water to produce a supersaturated fcc solid solution. Samples were then aged from 60 to 15840

sec at 950° C to produce intragranular laths of Cr-rich bcc precipitates in the fcc matrix. TEM samples were prepared by grinding samples to approximately 100 microns thick and punching 3 mm diameter disks. The disks were thinned using a South Bay model 550-C single jet polisher in a solution[46] containing (by volume): 7% perchloric acid, 11% 2-Butoxyethanol, 31% N-type Butanol, 51% Ethanol. Polishing was carried out at −30°C, 18 - 20 mA current (approximately 200 V - 240 V) , pumping rate setting of 1 and sensitivity setting of 0.5, respectively. Experience showed that controlling temperature and current were particularly important to producing good TEM foils. Specimens were examined at room temperature and during precipitate growth with a hot-stage using a Philips EM420 transmission electron microscope operating at 120 kV.

Bcc precipitates formed by aging Ni–45 wt% Cr at 950° C are lath-shaped with the characteristics reported by Luo and Weatherly[16, 17]. The laths adopt the Kurdjumov-Sachs orientation relationship and their broad face (hereafter called face 3) lies close to a $\{112\}_{fcc}$ plane (the $(1\ \bar{2}\ 1)_{fcc}$ plane is used throughout the remainder of this paper) with little variation from one precipitate to another. The long side facet (hereafter called face 1) varies between the $(313)_{fcc}$ and the $(414)_{fcc}$ planes. Both face 1 and face 3 contain the crystallographic invariant line of the fcc→bcc transformation (approximately 5.19° from $[\bar{1}\ 0\ 1]_{fcc}$), so the long axis of the laths are parallel to the invariant line.

The width and thickness of precipitate laths were measured as a function of aging time from TEM micrographs taken of the laths in cross-section. The lengths of the laths were usually too long to permit observation in TEM foils. The influence of ledges on the shape of the precipitate during growth was evaluated by relating the heights and spacings of growth ledges in the precipitates boundaries to the dimensions of the precipitate. Care was taken to distinguish growth ledges from other types of interfacial defects. Each interphase boundary was observed in three non-coplanar zone axes: $\langle 110\rangle_{fcc}$, $\langle 112\rangle_{fcc}$ and $\langle 100\rangle_{fcc}$ under two-beam conditions. Defects in the interphase boundary that were observed to move relative to a reference point when the TEM foil was heated in a hot-stage were identified as growth ledges.

The ledge heights were measured by one of two methods. When the ledge risers were parallel to the electron beam, the ledge heights could be measured directly from micrographs. When the ledges were not parallel to the beam, their heights were estimated from the displacement of interface thickness fringes using the relationship[47]: $h = m \sin\beta \sin\phi$, where m is the fringe displacement, β is the angle between the boundary and the foil surface, and ϕ is the angle between the fringe and the boundary line.

A total of 367 precipitates from seven different aging times were observed. Of these, 121 precipitates could be tilted to an edge-on orientation to permit accurate determination of the precipitate's thickness and width using magnifications between 62,500 and 105,000 times.

At each aging time, the measured precipitate width, thickness, and number of ledges per unit length of facet were grouped into size classes. The number of observations in each size class were fit to a Gaussian distribution from which the mean and standard deviation of the precipitate width, precipitate length, or ledge spacing were determined. The mean values of these quantities are reported with 95% confidence limits.

3.4 Results

The morphology of the precipitate changes during the growth process, as can be seen in Figures 3.1 (a)-(d). After aging for 60 sec at 950° C, the bcc precipitate has already developed a distinct habit plane (face 3) but its edges are smoothly curved (Figure 3.1(a)). By 120 sec, a distinct side facet (face 1) appears and by 3600 sec it is well-developed on almost all precipitates (Figure 3.1(b)). The precipitates have a parallelogram-shaped cross-section during this period. A cusp forms in face 1 upon continued aging (Figure 3.1(c)). The development of the cusp in face 1 is a common feature during the growth of the bcc precipitates. The cusps begin appearing at 4200 sec at 950° C and 40% of the precipitates are cusped by 15,840 sec. A new facet formed accompanying with development of cusp in face 1 is the $\sim (\bar{2}1\bar{2})_{fcc}$ which may result from accumulating of the growth ledge [48].

An O-lattice calculation shows the facet is 9° away to the best matching plane in this system[49].

Growth ledges originate at the two edges of the precipitate that form the acute angles between faces 1 and 3 as shown schematically in Figure 3.2(c) and at two acute corners of the precipitate in Figure 3.3 (a). They move laterally away from these two edges along both face 1 and face 3.

Two types of ledges were observed during precipitate growth. One is straight and exhibits strong image contrast. The arrows in Figure 3.3 (a) indicate a series of these straight ledges, marked as "S", on face 1 and face 3. They are almost always perpendicular to the intersection of the foil surface and the precipitate edge. Their height was measured to be 0.9 nm, as shown in Figure 3.2 (a) (c), in agreement the earlier work of Luo and Weatherly[17]. However, the ledge heights in face 1 increase to $5 - 10$ nm at about the aging time when the cusp in this face forms, as shown in Figure 3.2 (a) (c). The intersection of the riser and terrace of this type of ledge is roughly parallel to $[\bar{1}\ 0\ 1]_{fcc}$ (close to the invariant line direction).

The second type of ledges are indicated by arrows with a letter "L" in Figure 3.3 (a). These ledges are also straight and appear on both face 1 and face 3, but they usually lie approximately $10-30°$ off the $[\bar{1}\ 0\ 1]_{fcc}$ direction and exhibit weaker contrast than the first type of ledge. Estimating from the displacement of interface fringes they produce, their height is also ~ 0.9 nm.

In the rare instances when face 3 was contained within the foil and oriented nearly perpendicular to the electron beam, the ledges had an irregular, curved appearance (arrows with a letter "C" in Figure 3.3 (b)). The "S" and "L" ledges may be simply different segments of these curved ledges. Because of the difficulty in obtaining face 3 interfaces with this orientation, accurate heights and spacings of the curved ledges were not obtained.

The "S" and "L" types of ledges were identified as growth ledges because their relative location in the interface was observed to change after heating samples to 565°C. Figure 3.4 shows two ledges indicated by arrows on face 3 had moved out of the interphase boundary

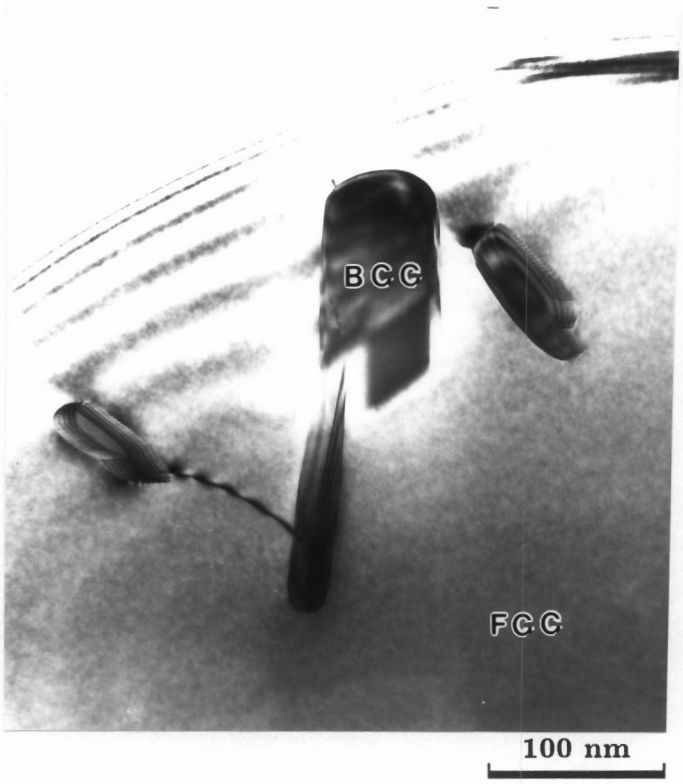

(a)

Figure 3.1: Morphology development of precipitates during growth. (a) A 60–second–aging precipitate with smoothly curved edges and a pair of facets (face 3). (b) By 2160 seconds precipitates finished faceting, an example of faceted precipitates was taken at 2160 seconds. (c) Cusped precipitates started forming on face 1 from 4200 seconds, an example was taken at 8160 seconds.

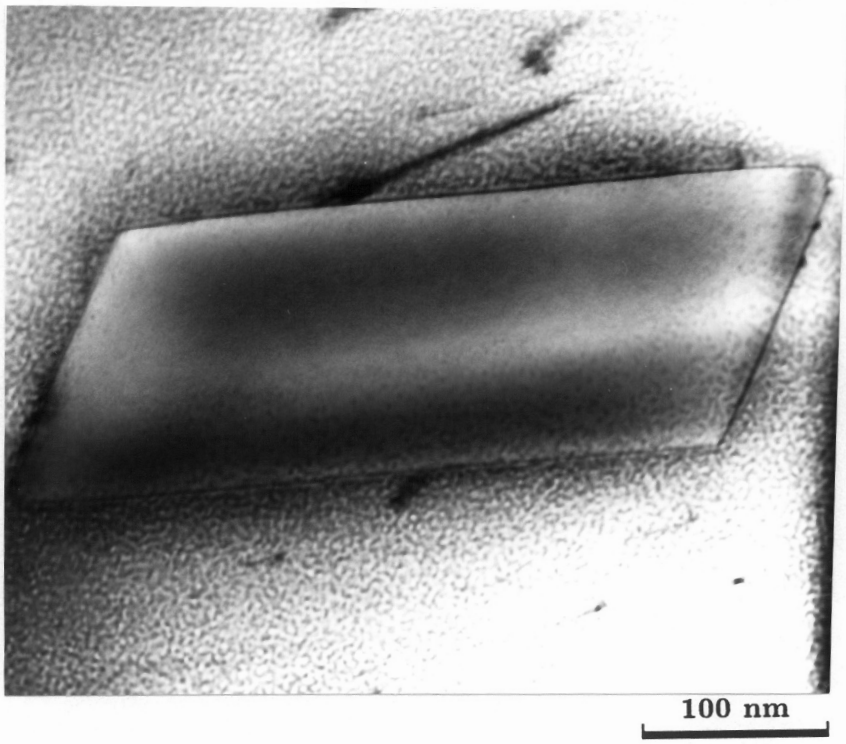

(b)

Cont. Figure 3.1 (b)

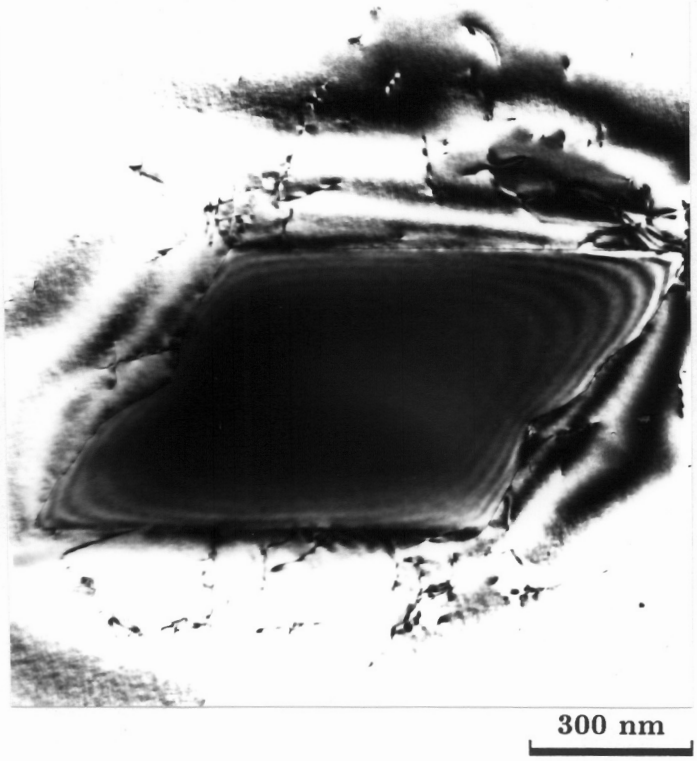

(c)

Cont. Figure 3.1 (c)

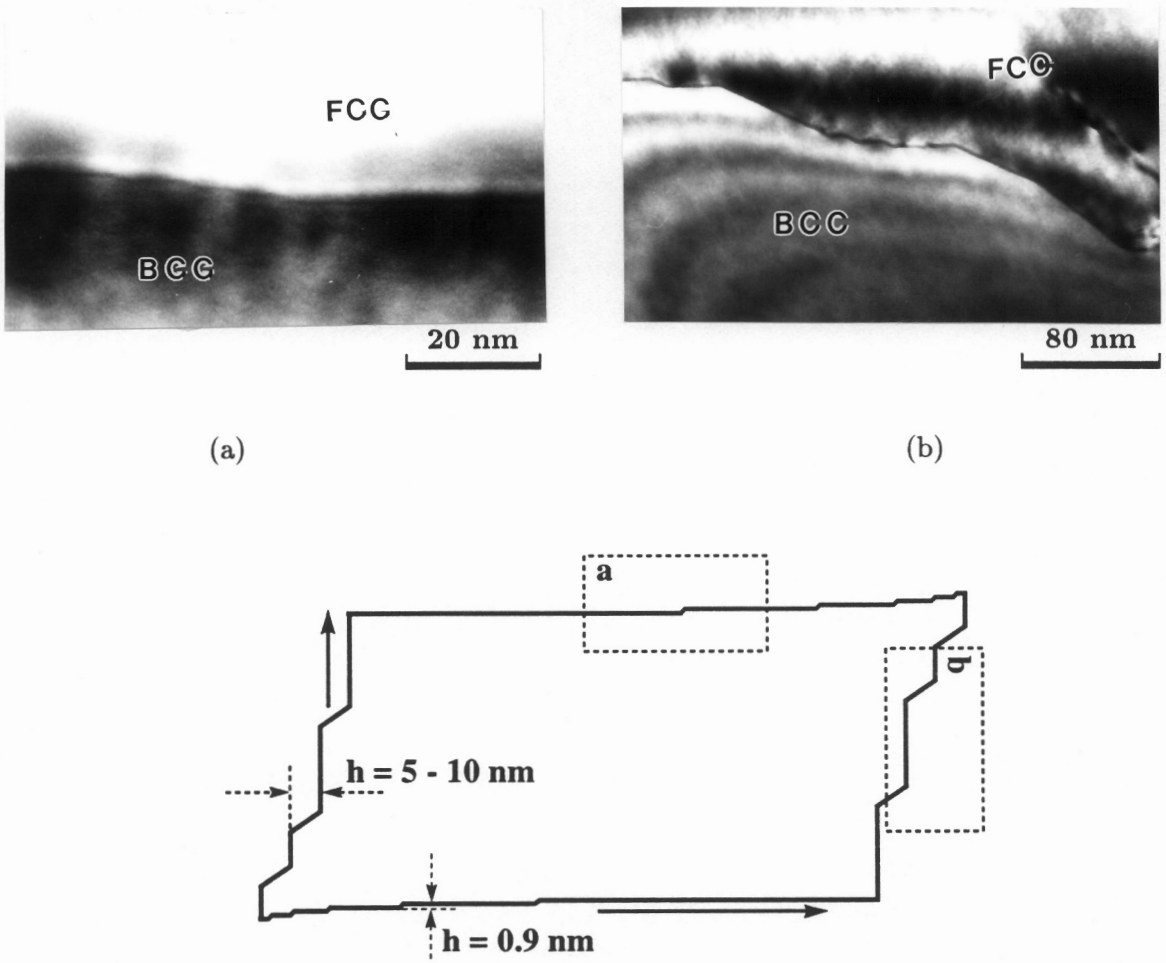

Figure 3.2: Development of ledge hight on face 1 of edge–on precipitates during growth. (a). Ledge heights on faces 1 & 3 measured were about 0.9 nm at early aging time. (b). Ledge hight on face 1 aged at 15840 seconds was measured from 5 nm–10 nm. (c). Schematic drawing for two independent sets of growth ledge on face 1 & face 3, the arrow shows lateral motion direction of ledges.

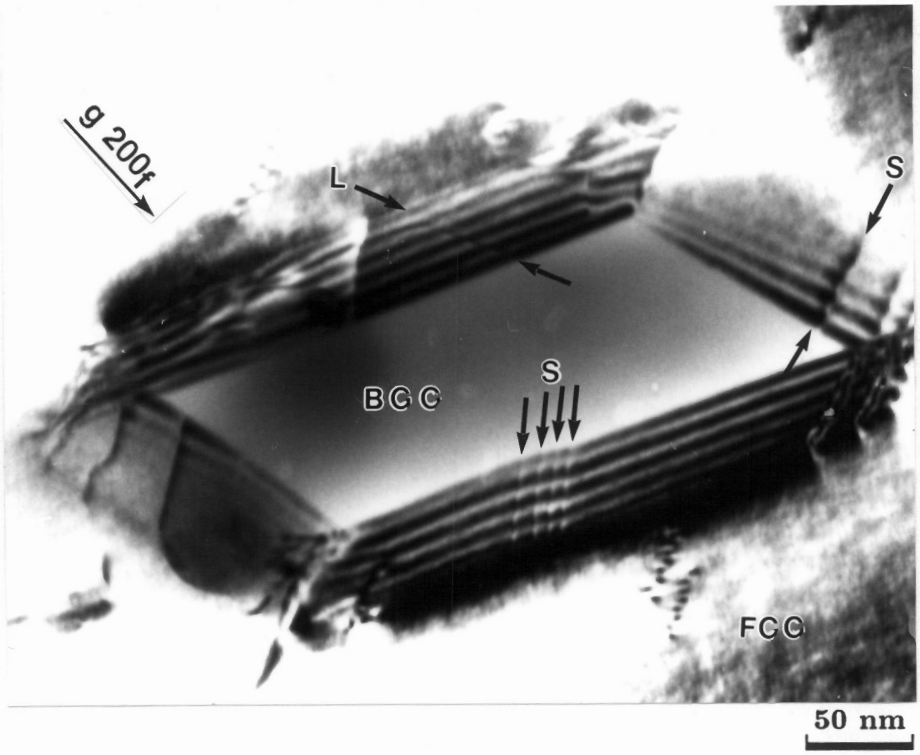

(a)

Figure 3.3: Bright field images of ledge types are: (a) A series of ledges with short and straight line (with arrows marked as a letter "S") on facet 1 and facet 3 of the precipitate, and the second type ledges (marked as a letter "L"), its length is much longer than "S", and usually inclined to the intersection of the foil surface and the precipitate edge. (b). The curved ledges (along arrows marked as a letter "C") have an irregular spacing, curvy appearance, and with weak contrast.

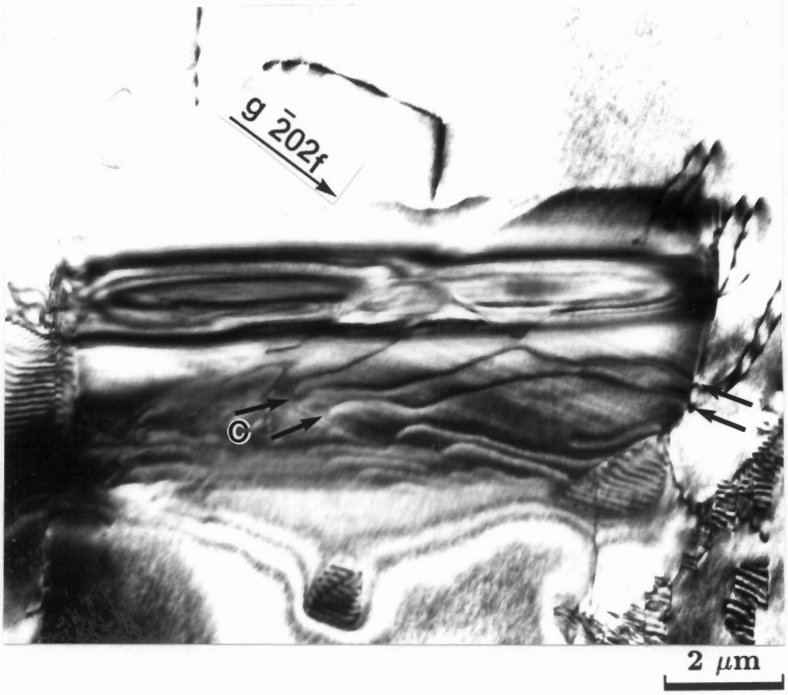

(b)

Cont. Figure 3.3 (b)

(in Figure 3.4(d)) when TEM foil was heated to 565°C for 180 seconds in the single tilt hot–stage holder. Both sides of the foil were covered by high purity Ti foil in order to prevent oxidation of the foil surface during *in situ* hot-stage. Figures 3.5 are two micrographs, one bright field showing a ledge with arrows on face 1 (Figure 3.5(a)) and the other is a weak beam dark field image showing the ledge has gone after being heated at 565°C for 60 seconds (Figure 3.5(b)).

One set of line defects observed also in this investigation has completely different features and functions from the growth ledges stated above. This type defect is the regular array of misfit dislocations with uniform spacings on face 1 and at the curved edges of face 1. The interfacial dislocations were reported to have a $\frac{a}{3}[1\bar{1}1]_{fcc}$ Burgers vector compensating misfit on face 1[16, 17].

The density of the ledges in face 1 and face 3 was determined by dividing the number of ledges in a given face by the length of the facet. Roughly 70% of the ledges counted were of the type that exhibit strong image contrast and are oriented along the invariant line. Figure 3.7 shows how the density of all types of ledges on the two growth interfaces varies with time. The ledge density on face 1 is roughly ten times greater than that on face 3. The densities on both faces were observed to decrease with aging time. The ledge density did not exhibit a maximum (minimum in ledge spacing) as has been reported to occur in other systems[5].

The kinetics with which the precipitate laths thicken and widen were determined from TEM micrographs of laths aged for different times. To avoid the need for stereological corrections, measurements were made only on those laths that could be tilted "edge-on". In this orientation, the electron beam is oriented along the lath's long axis and the true thickness and width can be determined directly from the projected image. The thickness and width of the laths follow power law kinetics ($s = \alpha t^n$) with exponents of 0.48 and 0.54, respectively. Least-squares fits of the kinetics data to $s = \alpha t^{0.5}$ growth laws yielded 1.75 nm/$\sqrt{\text{sec}}$ for the thickening parabolic rate constant and 3.76 nm/$\sqrt{\text{sec}}$ for the widening rate constant.

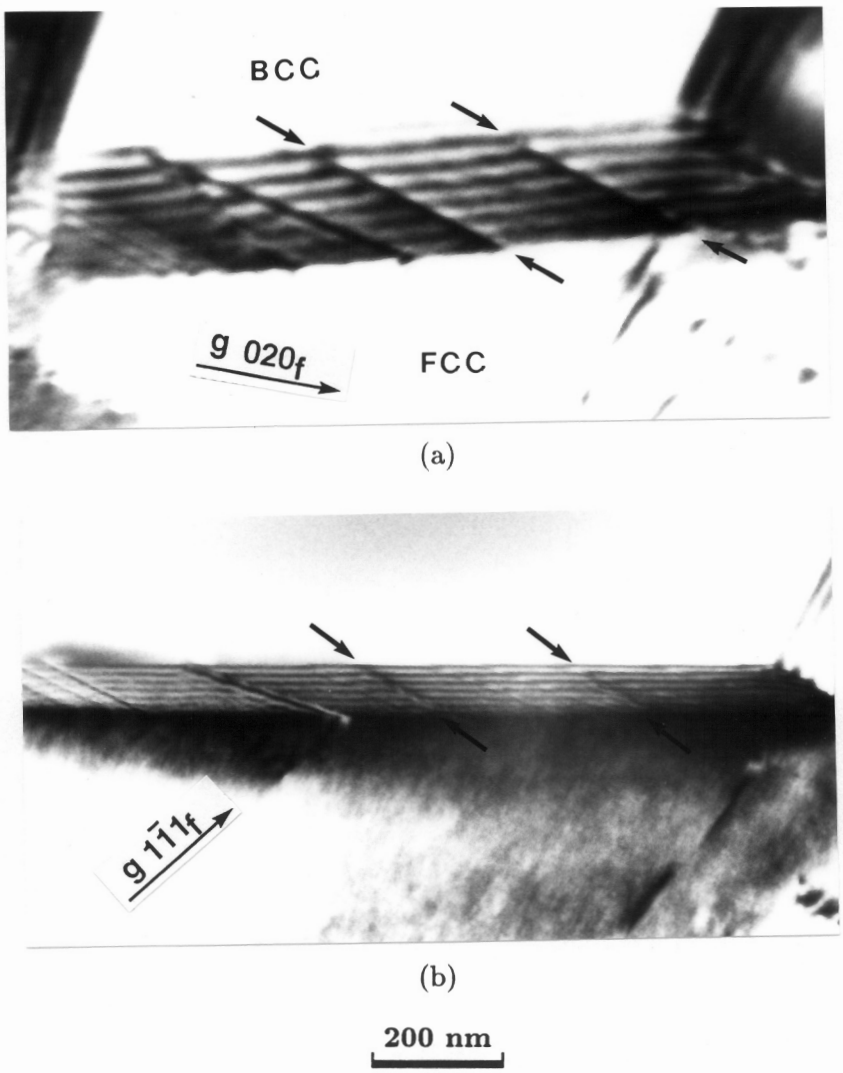

Figure 3.4: Comparison of TEM observations of growth ledges on face 3 at room temperature and in hot–stage at 565°C: (a) Bright field images taken at room temperature of growth ledges with arrows using $\sim [001]_{fcc}$ zone axes. (b) Another view using $\sim [\bar{1}01]_{fcc}$ zone axes. (c) Bright field images of face 3 with growth ledges in the hot–stage at 565°C using the same zone axes as in (b), heating time: 0 seconds. (d) The same condition as in (c) after heating for 180 seconds.

(c)

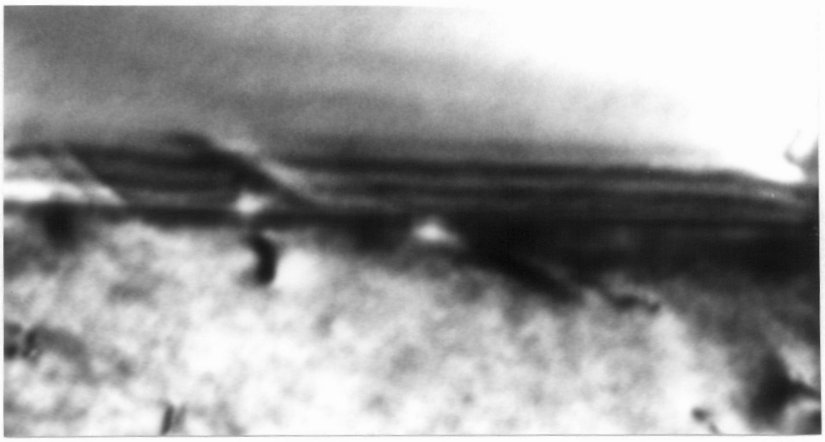

(d)

200 nm

Cont. Figure 3.4 (c), (d).

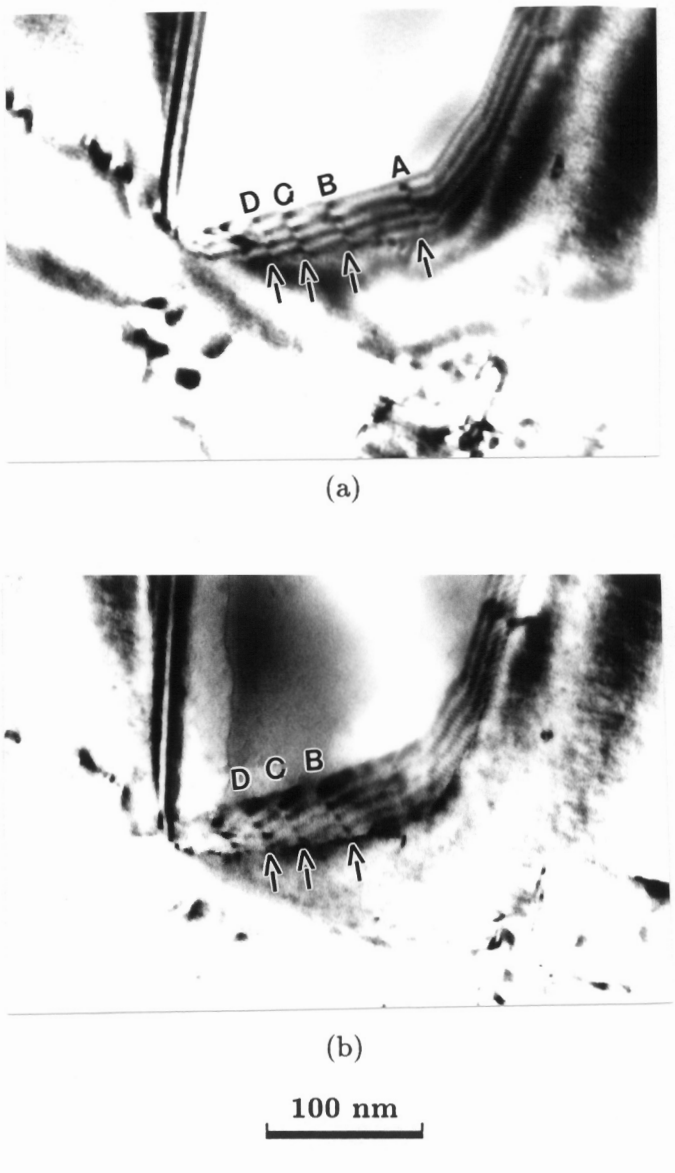

Figure 3.5: Comparison of TEM observations of growth ledges on face 1 at room temperature and in hot–stage at 565°C: (a) A bright field image taken at room temperature of growth ledges with arrows and marked with "A–D" using $\sim [\bar{1}01]_{fcc}$ zone axes. (b) A bright field image of growth ledges in the hot–stage at 565°C using the same zone axes as in (a) the ledge "A" disappears after heating for 60 seconds.

3.5 Discussion

The absence of obvious strain contrast associated with face 3 in Figure 3.1 (a) suggests that the precipitate is partially coherent after aging for 60 seconds. The appearance of an array of dislocation loops support this conclusion. At this stage of growth, face 3 on many precipitates is distinctly planar, but face 1 is not yet faceted. Face 3 on all of the precipitates is faceted for aging times greater than approximately 2000 seconds while face 1 does not complete faceting until 4200 seconds (Figure 3.1 (b)). Faceting of face 3 before face 1 can be explained by the relative misfit strains in the two interfaces.

Deviations of face 3 from the $(1\ \bar{2}\ 1)_{fcc}$ plane must be accomplished by the introduction of steps whose risers lie out of this plane. Since the misfit in these riser planes is greater than that in face 3 [49], these steps are relatively difficult to form. Steps on face 1, on the other hand, can have risers with relatively low misfit[49], so these steps are comparatively easy to generate. The resulting higher ledge density on face 1 leads to a lower tendency for this face to facet. The better atomic matching between the matrix and precipitate on face 3 thus may explain why the face 3 facets faster than face 1.

The development of the cusp in face 1 coincided with an increase in the height of the growth ledges on this face. An increase in height is likely to be a result of the coalescence of ledges. Such coalescence depends upon a number of factors: the formation rate of ledges, and their subsequent migration rate, as well as interactions between the elastic strain fields[48, 50] and the diffusion fields[51] of adjacent ledges. Coalescence of growth ledges is favored by low chemical supersaturations[51], high ledge formation rates, and/or a strong elastic repulsion between the growth ledges and the edge of the precipitate[50, 52, 33]. At the early stages of growth when cusping of face 1 occurs and ledge heights increase, the chemical supersaturation is expected to be relatively high. Thus, coalescence is likely to be due to a combination of high formation rates on face 1 and elastic interactions between ledges.

The present observation of the ledge origin is consistent with experimental observations

by Luo and Weatherly[17] who noted that the two broad facets of precipitates formed during aging of the same alloy at 1050°C contain ledges which rotate the two interface planes in the same direction. In Figure 3.1(c) it is indicated that ledges nucleated at opposite edges of the precipitate move in opposite directions and meet at the two remaining edges of the precipitate. A similar observation was made for ledges on Ω plates in an aluminum alloy[48]. Strain energy calculations[22] indicate the strain energy for ledge formation on bcc laths in Ni–Cr is centro-symmetric, and locations at opposite edges of the lath have the lowest strain energy. For one type of partial coherency, the minimum strain energy site for ledge formation is the corner of face 2 at the end of the edge where ledges were observed to originate in this study. This suggests that the local elastic strain field around the precipitate is a determining factor for the location of ledge nucleation.

The height of the growth ledges, which affects the migration rate of the interphase boundary, appears to be related to the crystallographic matching between the precipitate and the matrix phases and is thus system dependent. Table 3.1 shows observed features of growth ledges in a number of systems. It can be seen that ledge heights vary substantially—from several lattice planes to several thousand planes in height. While the larger ledges are almost certainly the result of coalescence of many smaller ledges, the height of the ledges responsible for growth is system dependent. A 0.9 nm ledge height on face 3 of the bcc precipitates in Ni–Cr corresponds to twelve $(2\ \bar{4}\ 2)_{fcc}$ planes (the atomic planes parallel to this habit plane), and fourteen $(3\ \bar{1}\ 2)_{bcc}$ planes. This height results in near-coincident sites between fcc and bcc at the top and bottom of the ledge riser. Heights greater or less than 0.9 nm yield significantly poorer matching. There is some residual misfit perpendicular to the habit plane associated with the ledges of this height on face 3. If this strain is not compensated by the creation of a misfit compensating defect in the ledge riser (as occurs for Ω precipitates in some aluminum alloys[48]), adjacent ledges will repel each other making coalescence difficult on face 3.

Interphase boundary matching in the risers of ledges on face 1 is better than that in risers on face 3. Using the same line of reasoning, coalescence is thus expected to be somewhat

Table 3.1: Geometric features of growth ledges in several systems

Precipitate	Location	Height (nm)	Spacing (nm)	Technique
θ' in Al-4%Cu [53]	plate edges	~ 2.3 and 0.6		Hot-stage TEM
γ in Al-15%Ag [21]	plate edges	$10-50$	$4-10$	Hot-stage TEM
ferrite laths in Fe-C [18]	broad faces	$42-1600$	$20-1300$	THEEM
ferrite in Fe-C-Si [27]		<3	<3	Hot-stage HVTEM
α plates in Ti-6.62at%Cr [54]	broad face	$\gg 7$	irregular	Hot-stage TEM
Ω plates in Al–Cu–Mg–Ag [48]	broad face	$0.45, 1.7-2.5$	$>4.5, >10$	TEM
β laths in Ni-45wt%Cr [16, 17] , this work	edges, broad face	0.9	24–1300	Hot-stage TEM

easier on face 1 as evidenced by the increase in ledge height at the onset of cusp formation.

The spacing of growth ledges, or the reciprocal of ledge density, is another geometric parameter directly related to the growth kinetics[5]. In contrast to the uniform spacing of the structural ledges[2], the spacings of growth ledges are usually irregular, as shown in Figure 3.3. In Table 3.1 it can be seen that the spacings during different growth stages vary. Several investigators[2, 55, 56] concluded the spacings were large at an early stage of growth, went through a minimum, and rose again during later stages of growth. It was suggested that the minimum in ledge spacing was related to an insufficient supply of the ledges at later reaction times. The present observations indicate: (1) the distribution of ledge spacings on bcc precipitates in Ni–Cr at all aging times is irregular; (2) there are difference ledge spacings on face 1 and face 3; (3) the closer ledge spacings occur near the ledge nucleation sources (usually at the corners or cusps of precipitates); and (4) the spacing increases monotonically (the ledge density decreases) on both of face 1 and face 3 with aging time.

Much of the prior observations of ledge growth rates were made using thermionic emission electron microscopy (THEEM) of the broad faces of ferrite plates in steels[18, 19, 20]. Significant differences between those results and the present observations are: (1) Average thickening kinetics of ferrite plates are erratic and exhibit either linear, parabolic, stepped kinetics or combinations thereof. This lead the earlier workers to suggest interfacial structure plays a crucial role in ledge migration kinetics. (2) Ferrite growth rates are generally much slower than those calculated for a planar disordered interface[18]. (3) Ferrite ledge heights (42 to 1600 nm) and spacings (200 to 13500 nm) are 2-3 orders of magnitude greater than those of the present investigation. The higher supersaturation for ferrite growth compared to that operative in the present case may explain some of these differences. The last difference may be due, in part, to the limited resolution of the THEEM technique and its inability to resolve small growth ledges before coalescence.

The growth kinetics of the bcc laths are considered first from the point of view of the overall widening and thickening rates, and then from the perspective of ledge formation and

migration. The kinetics of thickening and widening are compared in Figure 3.6 to growth models constructed using the assumption of diffusion controlled kinetics with no barrier to boundary migration (disordered boundary assumption). For a planar interphase boundary, the kinetics are described by the expression[57, 58]:

$$\begin{aligned} \frac{\alpha}{2\sqrt{D}} \exp\left(\frac{\alpha^2}{4D}\right) \operatorname{erfc}\left(\frac{\alpha}{2\sqrt{D}}\right) &= \frac{1}{\sqrt{\pi}}\left(\frac{C_o - C_\alpha}{C_\beta - C_\alpha}\right) \\ s &= \alpha\sqrt{t} \end{aligned} \tag{3.1}$$

where α is the parabolic rate constant describing the location, s, of the interphase boundary as a function of the growth time, D is the interdiffusion coefficient (estimated from diffusivity data for Ni and Cr[59] to be 162 nm^2/sec at 950°C), and $\frac{C_o - C_\alpha}{C_\beta - C_\alpha}$ represents the fractional supersaturation (0.11 at 950°C). Equation 3.1 was solved numerically for the parabolic rate constant yielding $\alpha = 1.72\ nm/\sqrt{sec}$. This value is quite close to the experimental value for thickening ($1.75\ nm/\sqrt{sec}$) but less than half the value for widening ($3.76\ nm/\sqrt{sec}$).

If one treats the thickening and widening process as the growth of an oblate ellipsoid of revolution, the kinetics can be described by the expression[60]:

$$\begin{aligned} 2\exp(\Omega)\,\Omega^{3/2}\left(\frac{\exp(-\Omega)}{\sqrt{\Omega}} - \sqrt{\pi}\operatorname{erfc}\left(\sqrt{\Omega}\right)\right) &= \left(\frac{C_o - C_\alpha}{C_\beta - C_\alpha}\right) \\ \alpha_{\text{thickening}} &= 2\sqrt{\Omega D} \\ \alpha_{\text{widening}} &= 2R\sqrt{\Omega D} \end{aligned} \tag{3.2}$$

where Ω is the single parameter used to describe growth and R is the aspect ratio (≈ 2). Ω is the only unknown in Equation 3.2. Solving for Ω yields parabolic rate constants for thickening and widening of 7.70 and 15.4 $nm/\sqrt{sec}$, respectively. The measured widening kinetics fall somewhat below those predicted by the oblate model.

From a mechanistic point of view, the interphase boundary is not disordered, nor can it migrate without the aid of growth ledges. The overall migration kinetics of the boundary thus depends upon the formation rate, f and the height, h, of ledges[3, 4]:

$$G_L = f\,h \tag{3.3}$$

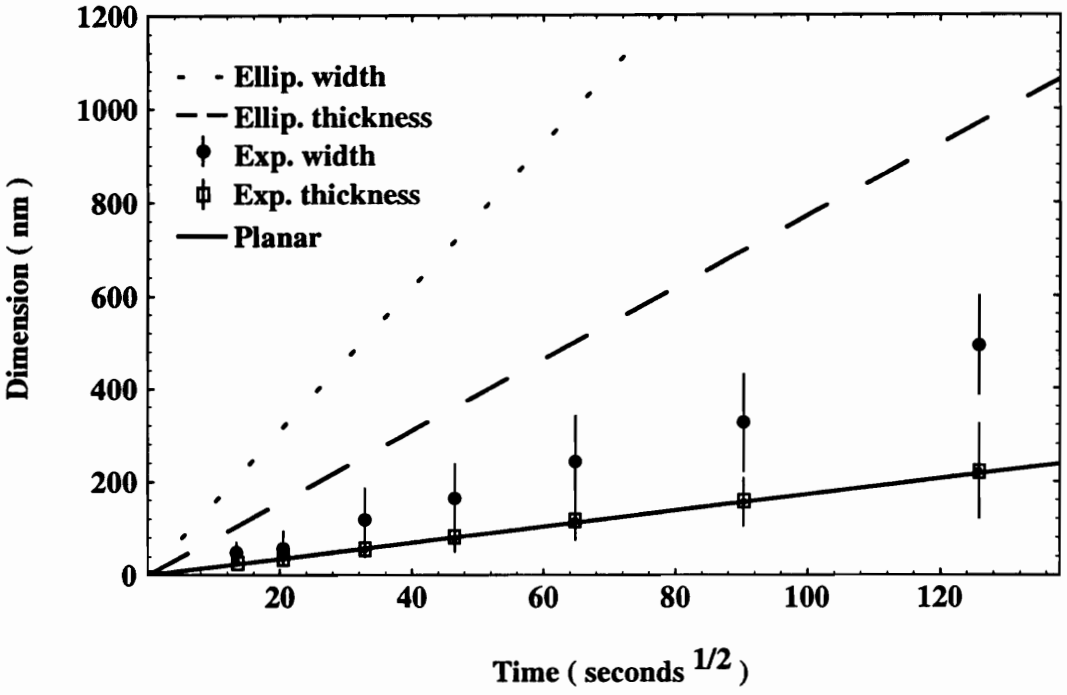

Figure 3.6: Comparison of growth constants calculated using disordered planar boundary and oblate ellipsoid boundary with experimental data of precipitate thickening (squares with error bars, 1.75) and widening (solid points with error bars, 3.62), the solid line represents the disordered planar model calculation (1.71), the dashing line is oblate ellipsoid thickening (7.77) and the dot line refers to oblate ellipsoid widening.

The fact that the measured kinetics are comparable to those predicted by the planar and oblate models implies that the formation rate of ledges follows parabolic kinetics with the individual ledges moving at diffusion controlled rates. This can be described alternatively by the spacing of adjacent ledges. When a ledge forms before its predecessor has a chance to migrate to the end of the facet, the formation rate is approximately $f = \frac{V_l}{\lambda}$ where λ is the interledge spacing. Enomoto[28] has shown numerically that ledged boundaries migrate with approximately the same kinetics as disordered boundaries when $\frac{h}{\lambda}$ is small.

The different migration kinetics of face 1 and face 3 suggest that there is a different kinetic barrier to growth on these two facets. Since the initial ledge heights are the same on the two faces, the formation rates of the ledges must differ. Since the measured overall growth rate on face 1 is about twice faster than that on face 3, $G_1 > G_3$. Applying Equation 3.3 separately to face 1 and face 3 with $h_1 = h_3$ indicates f_1 must be greater than f_3. This is supported by the observation of more closely spaced ledges on face 1 than on face 3 (Figure 3.7). More rapid ledge nucleation on face 1 translates into a higher migration rate for this facet, or, in the context of the general theory for precipitate morphology[1, 2], a higher apparent mobility. The higher formation rate for ledges on face 1 is likely to be related to the comparatively lower interfacial energy associated with ledge risers on this face and a lower elastic strain energy associated with these ledges. Assuming that a new ledge nucleates on face 1 and face 3 with the same volume, the energy required for ledge nucleation consists of the interfacial energy of ledge risers and the accompanying strain energy. The risers of ledges on face 1 are parallel to face 3 while the risers of ledges on face 3 are parallel to face 1. Since the atomic matching in face 3 is better than that in face 1[49], ledges with face 3 risers are likely to have lower interfacial energy barriers to nucleation. Thus, ledges forming on face 1 should form with greater kinetics than ledges on face 3.

The velocity of the ledges can be estimated by substituting $\frac{V_l}{\lambda}$ for f in equation 3.3 and rearranging:

$$V_l = \frac{\lambda G_L}{h} = \frac{\alpha\lambda}{2ht^{1/2}} \tag{3.4}$$

The last equality is the expression for the growth rate in terms of the measured parabolic

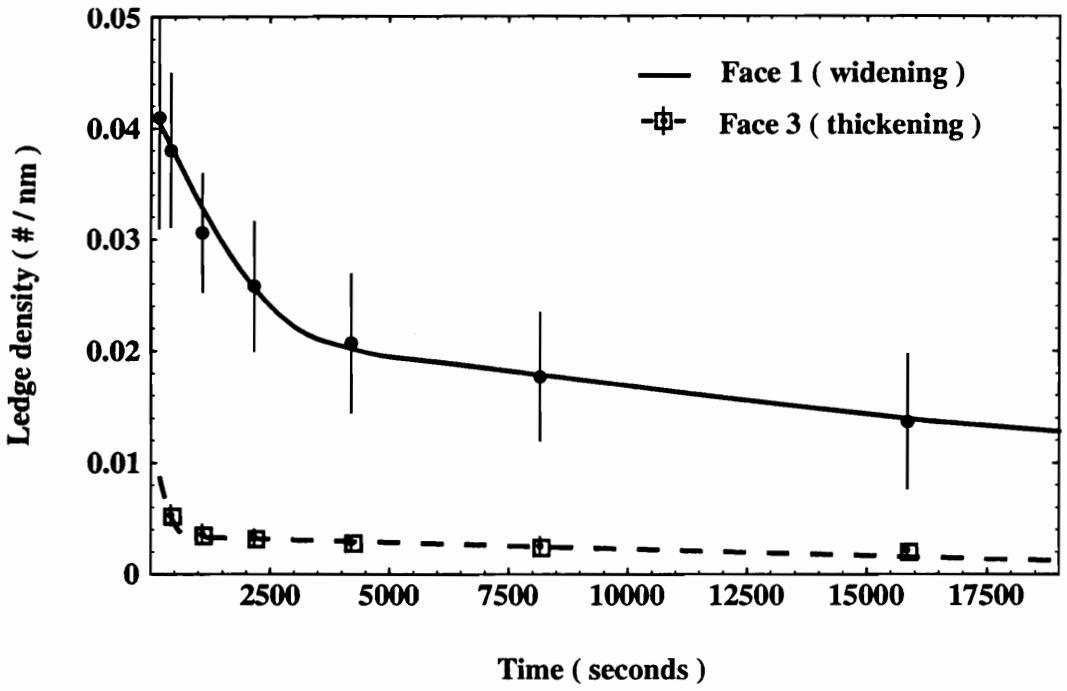

Figure 3.7: The average ledge density as a function of aging time with 95% confidence limits denoted by the error bars. Average densities of total ledges *verse* aging time on facet 1 (widening, solid line) and on facet 3 (thickening, broken line).

rate constant. For a ledge height of 0.9 nm and the measured ledge densities (inverse spacings), the ledge velocities range from 14-17 nm/sec on face 1 and 11-16 nm/sec on face 3. These approximate values for the ledge velocities can be compared with several analytical models for diffusion-controlled ledge migration[61, 62]. When the ledge spacing, λ, is large enough that the ledge velocity is not altered by the presence of neighboring ledges, these models predict a ledge velocity of 19.4 nm/sec. This agreement is somewhat surprising. The measured ledge velocities do not change much despite changing reaction times and ledge spacings. This implies that the ledge spacing is large enough that adjacent ledges do not interact diffusionally, and the ratio, $\frac{\lambda}{\sqrt{t}}$, is constant.

A mathematical model describing step kinetics during volume diffusion-controlled lateral growth have been proposed by Jones – Trivedi – Atkinson[61, 62]. Assumptions of a constant flux of solute at the ledge riser and zero flux at the ledge terraces were employed for modeling the migration of an isolated ledge. Since a time-independent diffusion field at the moving ledge was assumed, a steady-state ledge velocity was obtained. The ledge velocity may be calculated when ledge height, solute supersaturation and interdiffusivity are known by the equation given[61, 62]:

$$V_l = \frac{D}{h\alpha(p)} \frac{C_o - C_\alpha}{C_\beta - C_\alpha} \tag{3.5}$$

where V_l and is the ledge velocity, D, h, C_o, C_α, and C_β are defined as before, the $\alpha(p)$ represents an effective diffusion distance[61, 62]. When the average value of the ledge spacing λ is assumed to be large enough so that the ledge velocity is not altered due to the presence of neighboring ledges. The Equation 3.5 becomes[61, 62]:

$$p = \frac{V_l h}{2D} \tag{3.6}$$

where the p is Peclet number, a dimensionless velocity parameter. Assuming the interface boundary has high mobility or high kink density the p can be estimated as 0.0538 from the plot of $\log p \, vs \, \Omega$[61, 62] for a supersaturation of 0.11. The ledge velocity predicted by the Jones–Trivedi model was then calculated by using the h and D values mentioned above. The results are shown in Table 3.2 where they are compared with measured V_l value. Assuming

a planar, disordered interface the measured ledge velocities were obtained using derivation below [57, 63]:

$$s = \alpha t^{1/2} \tag{3.7}$$

where s is the growth length, α is the parabolic growth constant and t is reaction time. The growth velocity can be derived by differentiation of s with respect to time, t :

$$G = \frac{ds}{dt} = \frac{\alpha}{2t^{-1/2}} \tag{3.8}$$

where the G is the growth velocity of the precipitate. And the relationship of the growth rate and the ledge lateral velocity was given in Equation 3.3. Replacing Equation 3.8 with G_L into the Equation 3.3, the ledge velocity can be obtained in the Equation 3.4. The α, λ, h and t were shown in *Results* section. Using these data the measured ledge velocity can be obtained. From the Table 3.2 it can be seen that the agreement between the ledge velocity calculated by the Jones–Trivedi model and measured by this procedure is very good. Suggesting the ledges migrate at diffusion–controlled rates.

3.6 Conclusions

1. Overall widening and thickening of bcc precipitate laths in Ni–45wt%Cr occur with diffusion controlled rates..

2. Growth ledges observed *in situ* hot–stage TEM are mobile although they have at least two different morphologies.

3. At early aging times the ledge height on both faces 1 and 3 is approximately 0.9 nm; at later aging times the height remains the same on face 3 but increases to $5 - 10$ nm on face 1 due to coalescence of ledges.

4. Spacings of growth ledges are usually are irregular, but increase with aging time.

5. Growth ledges nucleate at two opposite edges of the precipitate and move laterally in opposite directions.

Table 3.2: Comparison of parabolic growth constants in disordered boundary calculation, J–T–A ledge boundary calculation and experimental data

Boundary–type	α (nm/$\sqrt{\text{sec}}$)	Model
Planar	1.72	Dubé–Zener[57, 63]
Oblate, widening	15.40	Menon–et. al.[60]
Oblate, thickening	7.70	"
Face 1 ledged	3.7550	ledged growth [61, 62]
Face 3 ledged	1.8550	"
Face 1 (widening)	3.76	Experimental data
Face 3 (thickening)	1.75	"

6. The difference in the apparent mobilities of face 1 and face 3 is a result of a difference in the formation rate of ledges on these faces. Ledges form more readily and coalesce more easily on face 1. This is likely to result from a lower strain energy for ledge formation on face 1 due to better interfacial matching in the ledge riser.

Chapter 4

EXPERIMENTAL OBSERVATION ON EMISSION OF STRUCTURAL DEFECTS FROM PARTIALLY COHERENT INTERPHASE BOUNDARY

4.1 Introduction

The diffusion controlled growth of precipitates in many systems requires the displacement of partially coherent interphase boundaries. Migration of these boundaries is generally accomplished by a ledge mechanism in which mobile ledge risers advance over immobile ledge terraces. A fundamental gap in the understanding of the process is the way in which misfit compensating defects in the ledge terraces migrate with the boundary[29, 64].

Misfit compensating defects (either dislocations or steps) relieve the coherency strains at the boundary between dissimilar crystals. When a ledge riser advances over a terrace containing these defects, the terrace is effectively displaced a distance equal to the height of the riser. The misfit compensating defects, which are sessile except in special circumstances, must be transferred from the original terrace to the location of the new terrace, or an additional array must be generated at the new terrace. In the latter case, the old array must be removed in some way since they are no longer needed to accommodate misfit. In addition, if there is a difference in molar volume between the parent and product phases, the advance of the boundary and the disposition of the misfit compensating defects must be accompanied by a net flux of vacancies toward or away from the precipitate[65, 66].

One mechanism for emission of misfit dislocations from the boundaries has been proposed[67, 68, 69] based on TEM observations of the precipitation and dislocation nucleation in quench–

aged Al–Mg alloys[69], the thickening of γ plates in Al–Ag[21, 24, 25], the thickening of Θ' in Al–Cu[56, 70] and the thickening of ferrite plates in Fe–C alloys[18, 71]. Advancing ledges may cause misfit dislocations ahead of them to glide along the terraces until they reach the end of the precipitate. At this point they are ejected into the matrix, presumably as prismatic loops. Alternatively, the misfit dislocation may climb from one terrace to next. If misfit dislocations are rejected from the precipitate, new ones have been suggested to form at the top of the moving riser[67]. However, little direct evidence of the mechanism of the growth ledge or structural defect emission has been published so far. This work is an attempt to provide conventional and hot–stage TEM observations of defect emission from partially coherent precipitates during growth.

4.2 Experimental

The material, heat treatments, sample preparation methods and electron microscopy technique employed in this study were described in detail in chapter 3(see chapter 3). Briefly, a Ni–45wt%Cr alloy was aged for different times between 60 seconds and 15840 at 950° C. Specimens were electropolished and growth ledges, dislocations, and stacking faults on face 3[1] and face 1[2] were examined by conventional, *in situ* hot–stage, and high–resolution TEM using Philips EM420 and JEOL 4000 EX microscopes.

4.3 Results and Discussion

4.3.1 An array of loops glide off terraces into the matrix

Figure 4.1 shows bright-field TEM images of a precipitate aged for 60 seconds. The precipitate appears to be enclosed by an array of dislocation loops contained in face 3 ($(1\bar{2}1)_{fcc}$ habit plane) and face 1 ($\sim (313)_{fcc}$ habit plane)(see chapter 3). When the structural defects laterally moved on the habit plane the loops would glide off the interphase boundary.

[1]The present authors refer the broad face to the face 3, see[22]
[2]The present authors refer the side long face to the face 1, see[22]

Figure 4.1 (b) is another view of the same precipitate with a different zone axis. It can be seen that a dislocation (arrowed) seems to have migrate from the interface into the matrix. An array of dislocation pairs, marked "L", lies nearly in the matrix and appear to have originated in this manner.

An array of dislocations was found frequently in the immediate vicinity of the precipitates. While such an array can be expected to result when a precipitate initially loses coherency, dislocations should continue to be rejected as the precipitate grows. This was confirmed by *in situ* observations of the bcc precipitates during growth at 750° C (Figure 4.2).

Those loop-like defects were frequently observed in specimens aged at different times, as shown in Figures 4.3. Figure 4.3 (a) is an array of dislocation loops which may have been ejected from a nearby precipitate. Figure 4.3 (b) shows another similar array of closely spaced dislocation loops in a strong contrast. Some parts of the array have lost contrast, probably because of the collapse of the loops by dislocation climb. Figure 4.3 (c) is an edge–on view of the dislocation array shown in Figure 4.3 (b). The dislocations lie in a $\{111\}_{fcc}$ plane. Observations of this type of defect with HRTEM also indicates the dislocations are actually an array of very narrow loops (Figure 4.3 (d)). The area between the two arrows on either side of the figure corresponds to the thickness of the array in the edge–on orientation of Figure 4.3 (c). The crystal structure does not change across this region, so the contrast in Figure 4.3 (a)–(c) does not arise from a precipitate phase. These loops appear to be associated with the growth process and are probably formed either by prismatic punching of dislocation loops or by climb of dislocations to relax transformation stresses. Such phenomena have been reported earlier in Al–Mg alloys by Eikum et al[69].

4.3.2 Structural defects are rejected from terraces in the inclined direction to the broad habit plane

Rejection into the matrix of two types of dislocations from the interphase boundary has been observed in specimens aged greater than 8,160 seconds (Figure 4.4). The three

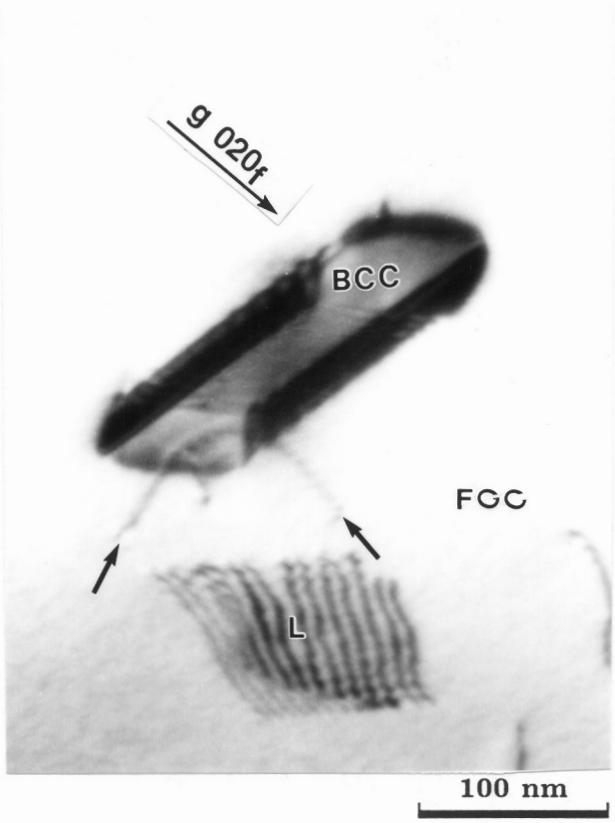

(a)

Figure 4.1: Dislocation loops from the precipitate glide off into the matrix. (a) A bright image with $[001]_{fcc}$ zone axis shows an array of dislocation loops are around of the precipitate, one loop (with arrows) is moving off the precipitate into the matrix and an array of dislocation loops left early during growth. (b) Another view of the precipitate bright image with $[1\bar{2}1]_{fcc}$ zone axis.

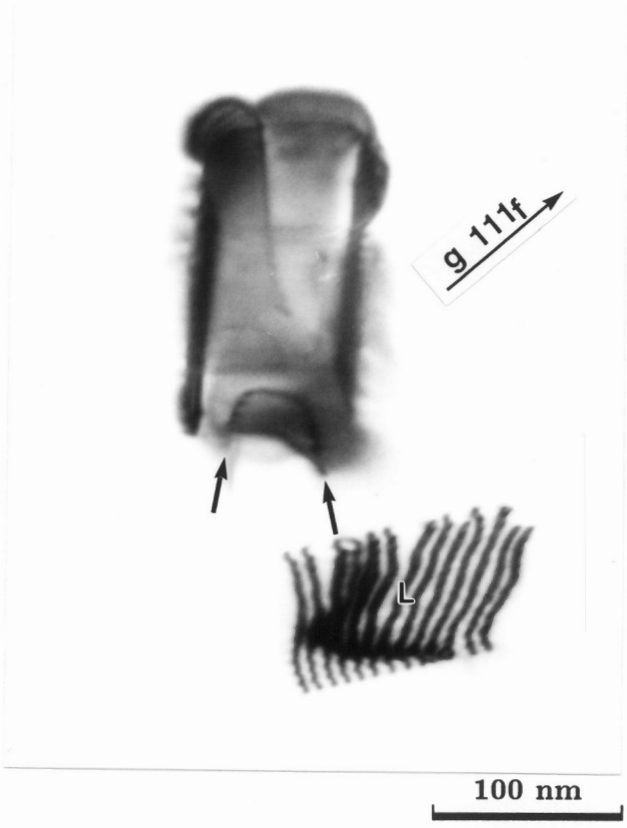

Figure 4.1 (b), cont.

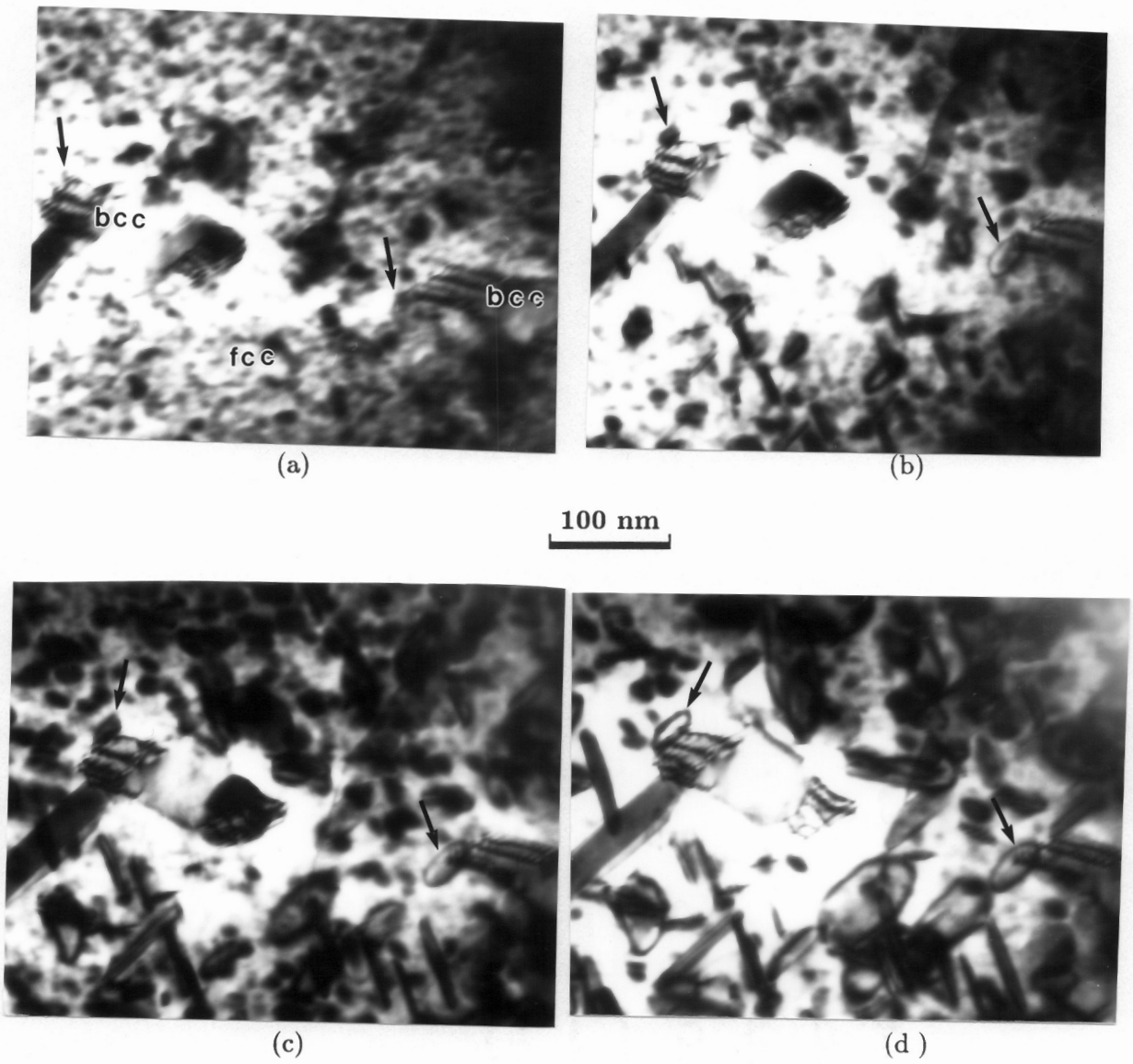

Figure 4.2: A series of *in situ* hot–stage TEM images taken at 750° C with aging time, two loops arrowed surrounding faces are expanding and gliding off the faces of the precipitate into the matrix. (a) Δ t = 0 seconds. (b) Δ t =900 seconds. (c) Δ t =1800 seconds. (d) Δ t = 2700 seconds.

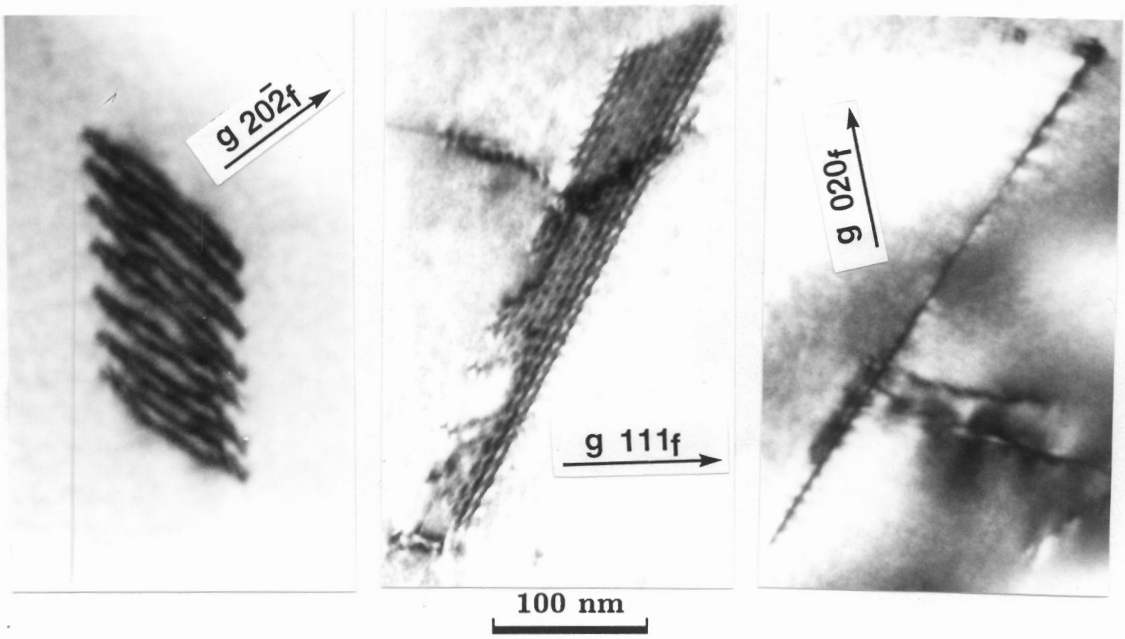

(a) (b) (c)

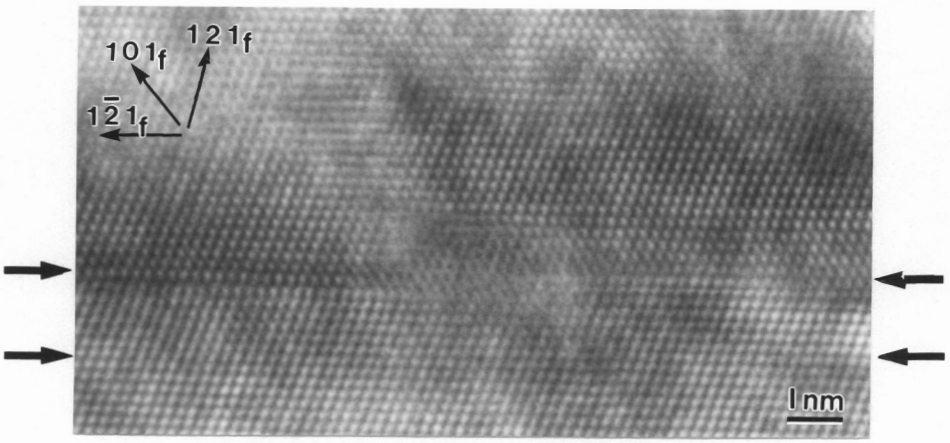

(d)

Figure 4.3: Several morphologies of dislocation loops and a HRTEM micrograph. (a) A bright image with $[1\bar{2}1]_{fcc}$ zone axis shows an array of dislocation loops were punched into matrix. (b) Another example of a dislocation loop array with $[1\bar{2}1]_{fcc}$ zone axis. (c) Edge–on morphology of the array in (b) with $[\bar{1}01]_{fcc}$ zone axis, the array lies on $\{111\}_{fcc}$. (d) HRTEM view of the dislocation loop array along the $[\bar{1}01]_{fcc}$ direction, the crystal structures between the region arrowed are the same as an fcc structure.

bright-field images were taken in a $[011]_{fcc}$ zone axis with $\mathbf{g} = [02\bar{2}]_{fcc}$, $\mathbf{g} = [\bar{1}\bar{1}1]_{fcc}$, and $\mathbf{g} = [200]_{fcc}$. Using the $\mathbf{g} \bullet \mathbf{b} \times \mathbf{u} = 0$ invisibility criteria, the dislocations were determined to have $\frac{a}{2}\langle 110 \rangle_{fcc}$ Burgers vectors. Two Burgers vectors were found for the dislocations coming from the interface of a single bcc precipitate. Dislocations labeled A, D, E, F and G in Figure 4.4 have a $\frac{a}{2}[1\bar{1}0]_{fcc}$ Burgers vectors and dislocations B and C have $\mathrm{b} = \frac{a}{2}[01\bar{1}]_{fcc}$. The dislocations often appear to emanate from face 3 (the $(1\bar{2}1)_{fcc}$ habit plane), and they lie in a $\{111\}_{fcc}$ plane.

4.3.3 Stacking faults interact with the interphase boundary

Figure 4.5 shows a set of stacking faults on face 3 of a precipitate aged for 4200 seconds. The four micrographs of Figures 4.5 are the same area under different diffraction conditions. The stacking faults were found at all the aging times investigated. In Figure 4.5 (a) it can be seen that there are 7 stacking faults emanating from face 3, marked "A" to "G". Figure 4.5 (b) is a dark field image with $\mathbf{g} = [020]_{fcc}$, Figures 4.5 (c) is a bright field image with $\mathbf{g} = [\bar{1}1\bar{1}]_{fcc}$ and Figures 4.5 (d) shows a dark field image with $\mathbf{g} = [111]_{fcc}$. Using trace analysis it was found that the stacking faults lie on the $(111)_{fcc}$ plane. Since width of the stacking faults is fairly narrow, about 10 nm, it was difficult to identify the bounding partial dislocations as either Shockley type ($\frac{1}{6}\langle 112 \rangle_{fcc}$) or Frank type ($\frac{1}{3}\langle 111 \rangle_{fcc}$) using conventional methods. Thus, it could not be ascertained whether the dislocations glide or climb into the matrix. From Figures 4.5 (b) an (c) it can be seen that except for stacking fault E, partials of each stacking fault lies in the interface. Both bounding partial dislocations of the fault marked "E" are completely out of the interphase boundary (Figure 4.5 (c)) and a ledge has been left behind in the boundary. In Figure 4.5 (d) clearly shows a line defect in the interface with a different contrast from the other partial dislocations where stacking fault "E" originated.

Shiflet has observed such stacking faults in austenite at the pearlite growth interface of Fe–C–Mn alloys[72]. A current study of atomic matching in face 3 indicates that the combination of an intrinsic stacking fault on the $(111)_{fcc}$ and an interface step improves

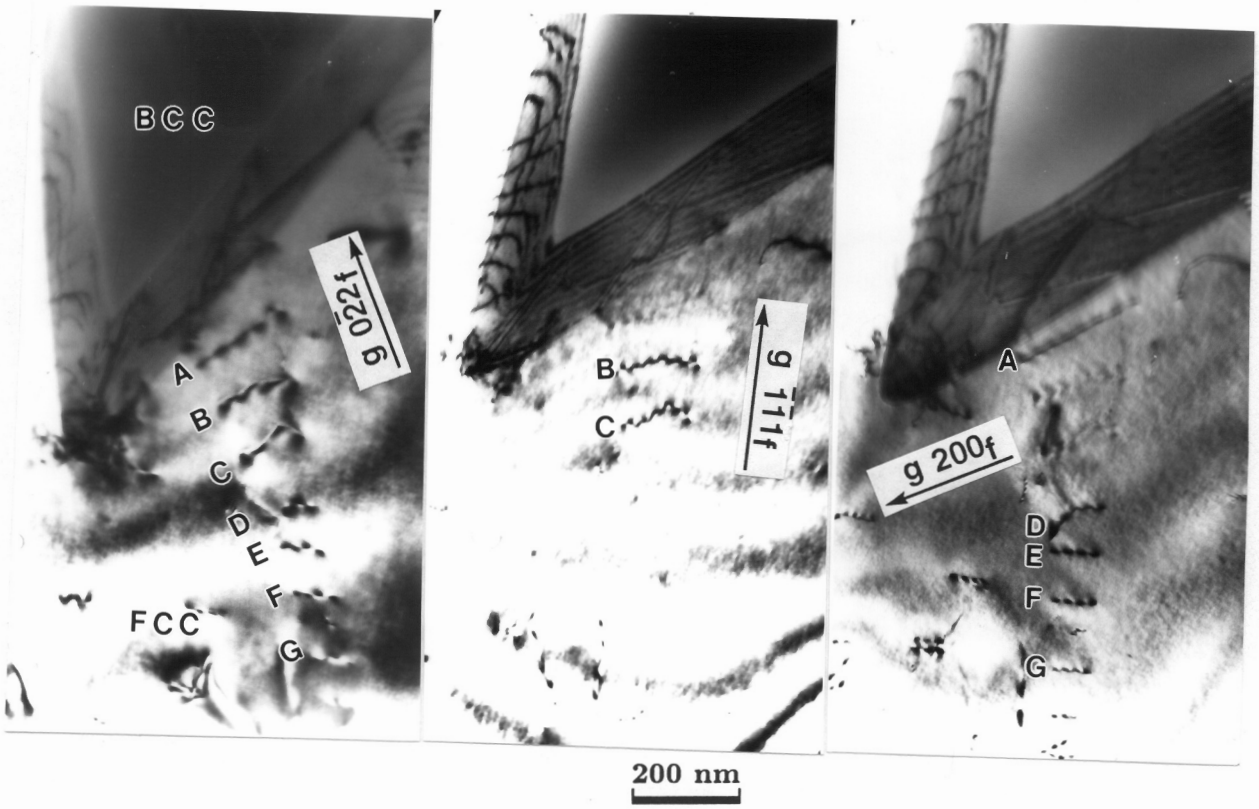

(a) (b) (c)

Figure 4.4: An array of Dislocations were rejected from the precipitate interphase boundary into the matrix. The dislocations marked "A","D","E","F" and "G" have a $\frac{a}{2}[1\bar{1}0]_{fcc}$ Burgers vectors, while "B" and "C" have a $\mathbf{b}$ of $\frac{a}{2}[01\bar{1}]_{fcc}$. Three different $\mathbf{g}$ vectors were used for the $\mathbf{g} \bullet \mathbf{b} \times \mathbf{u} = 0$ invisibility criteria; (a) $\mathbf{g} = [0\bar{2}2_{fcc}]_{fcc}$, (b) $\mathbf{g} = [\bar{1}\bar{1}1]_{fcc}$, (c) $\mathbf{g} = [200]_{fcc}$.

matching in the $(1\bar{2}1)_{fcc}$ habit plane[73]. However, the observation that ledges are left in the boundary when stacking faults leave the interface suggests that the faults also play a role in the formation of ledges.

4.4 Summary

1. Emission of dislocation loops from the fcc : bcc interphase boundary has been observed during the early stages of precipitation using conventional TEM and *in situ* hot-stage TEM technique.

2. At later aging times $\frac{a}{2}\langle 110\rangle_{fcc}$ type dislocations are rejected from $(1\bar{2}1)_{fcc}$ habit plane on a $\{111\}_{fcc}$ plane in the parent phase.

3. 1 & 2 are consistent with rejection of misfit compensating defects from interphase boundaries although it is not clear how this is done.

4. Stacking faults emanating from the fcc:bcc interphase boundary have been observed. The stacking faults may relieve misfit strain and lead to the formation of ledges in the interphase boundary.

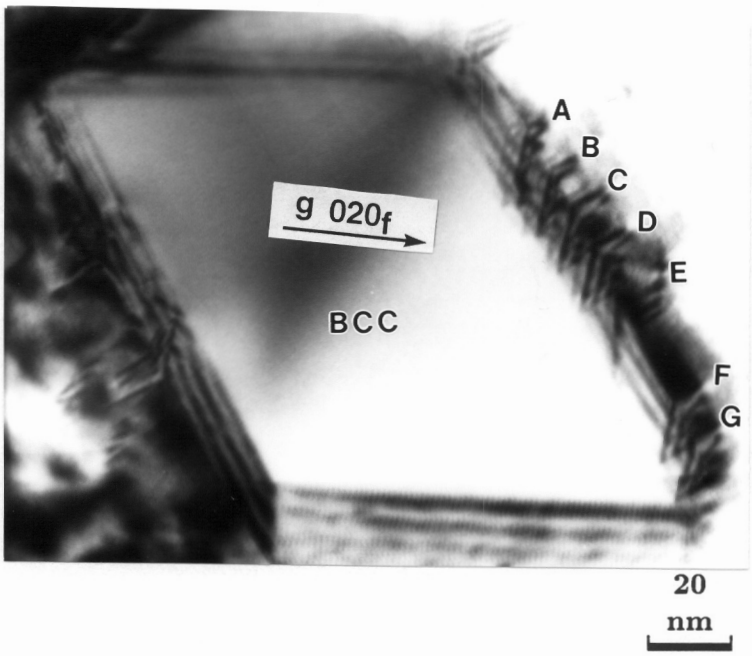

(a)

Figure 4.5: Stacking faults emanating from the interphase boundary of a precipitate. (a) A bright field image of the precipitate with 7 stacking faults on the face 3, marked "A"–"G". (b) Dark field image with $\mathbf{g} = 020$, the fault "E" is invisible. (c) Bright field image with $\mathbf{g} = \bar{1}1\bar{1}$ the fault "E" has moved out of the interphase boundary. (d) Dark field image with $\mathbf{g} = 111$, the "E" fault left one ledge (with different contrast and arrowed) on face 3.

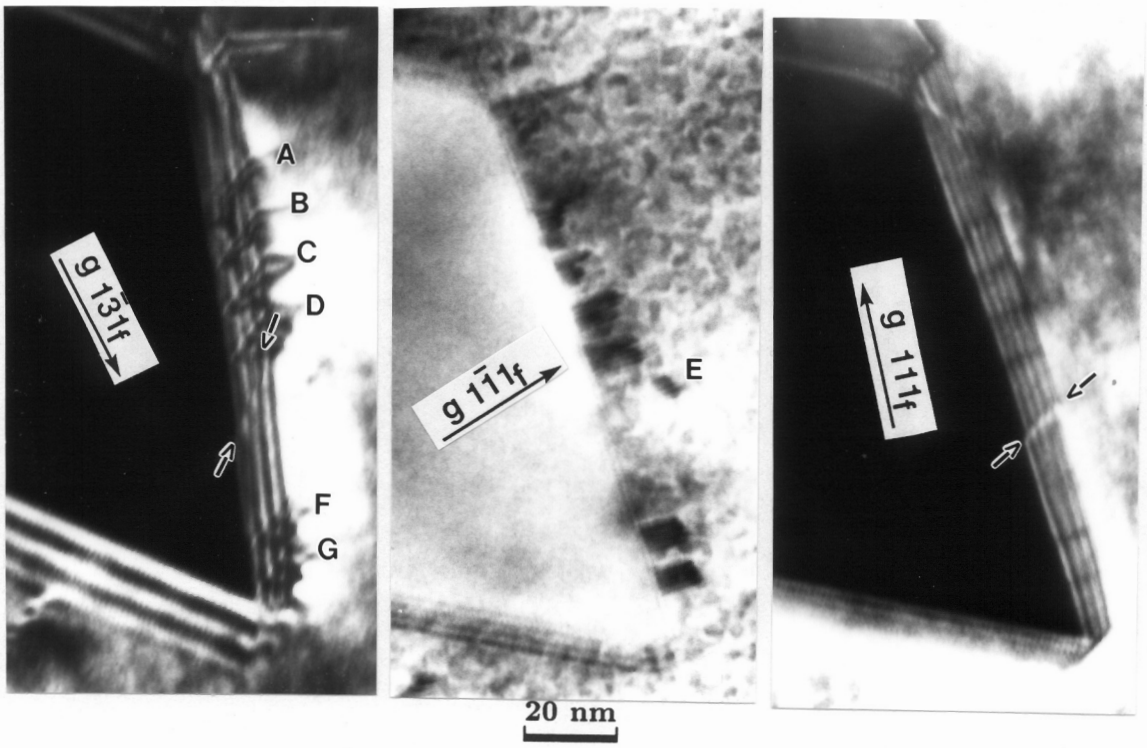

(b) (c) (d)

Figure 4.5 (b), (c) and (d), cont.

Chapter 5

SUMMARY

A systematic investigation on the role of ledges during the growth of a lath-shaped bcc precipitate has been carried out in a Ni–45wt%Cr alloy. The principal results are as follows:.

1. Ledge nucleation is only likely at facet areas where the interaction strain energy between the ledge and the precipitate is negative. The most favorable site for ledge formation from elastic strain energy considerations changes with coherency loss from the broad face (face 3) to the end face (face 2) and is sensitive to the nature of the misfit compensation. In general the strain energy for ledge formation is centrosymmetric about the lath and is lowest (and highest) along the edges of the lath.

2. At least two types of growth ledges were observed. More than 70% of the mobile ledges lie along the invariant line direction.

3. TEM observations indicate that growth ledges play a crucial role in the shape change of the precipitate when the lath loses coherency. Cusp formation on the edge of laths results from growth ledge coalesce and the development of an additional facet plane.

4. Overall widening and thickening of the laths are diffusion controlled with different rate constants. The anisotropic effective mobility of the two facet planes is a result of different ledge formation rates on these faces. Ledges form more readily and coalesce more easily on the edges of the laths (face 1). This is likely to result from a lower strain energy for ledge formation on face 1 due to better interfacial matching in the ledge riser. Although ledge formation rates were not measured on the ends of the laths (face 2), the greater migration rate of this boundary orientation implies that ledge formation is most rapid there.

5. Heights of growth ledges change with crystallographic orientations and aging time. At early aging times the ledge height on both faces 1 and 3 is approximately 0.9 nm; at later aging times the height remains the same on face 3 but increases to $5 - 10$ nm on face 1 due to coalescence of ledges.

6. Conventional TEM and *in situ* hot-stage TEM identified emission of dislocation loops from the fcc : bcc interphase boundary has been observed during the early stages of precipitation. At later aging times $\frac{a}{2}\langle 110\rangle_{fcc}$ type dislocations are rejected from $(1\bar{2}1)_{fcc}$ habit plane on a $\{111\}_{fcc}$ plane in the parent phase.

7. Stacking faults, which may contribute to misfit compensation in the broad face (face 3) of the lath, have been observed. The stacking faults are emitted from the interphase boundary and leave a ledge in the boundary.

REFERENCES

[1] H. I. Aaronson, in *The Decomposition of Austenite By Diffusional Processes*, V. F. Zackay and H. I. Aaronson, eds., Interscience, New York, 1962, pp. 387–549.

[2] H. I. Aaronson, C. Laird, and K. R. Kinsman, in *Phase Transformations*, H. I. Aaronson, ed., ASM, Metals Park, OH, 1970, pp. 313–396.

[3] J. W. Cahn, *Acta Metall.*, 1960, vol. 8, pp. 542–562.

[4] J. W. Cahn, W. B. Hillig, and G. W. Sears, *Acta Metall.*, 1964, vol. 12, pp. 1421–1439.

[5] H. I. Aaronson, *J. Microscopy*, 1974, vol. 102, pp. 275–300.

[6] R. M. Aikin Jr. and M. R. Plichta, in *Phase Transformations '87*, G. W. Lorimer, ed., The Institute of Metals, London, 1988, pp. 504–506.

[7] G. C. Weatherly, *Acta Metall.*, 1974, vol. 19, pp. 181–192.

[8] G. C. Weatherly, *Can. Metall. Quarterly*, 1969, vol. 8, pp. 105–109.

[9] K. A. Bywater and D. J. Dyson, *Metal Science*, 1975, vol. 9, pp. 155–162.

[10] U. Dahmen, *Scr. Metall.*, 1981, vol. 15, pp. 77–81.

[11] U. Dahmen, *Acta Metall.*, 1982, vol. 30, pp. 63–73.

[12] U. Dahmen, P. Ferguson, and K. H. Westmacott, *Acta Metall.*, 1984, vol. 32, pp. 803–810.

[13] U. Dahmen and K. H. Westmacott, *Acta Metall.*, 1986, vol. 34, pp. 475–482.

[14] U. Dahmen and K. H. Westmacott, in *Proc. Int. Conf. on Solid–Solid Phase Transformations*, H. I. Aaronson, D. E. Laughlin, R. F. Sekerka, and C. M. Wayman, eds., Warrendale, PA, 1983, pp. 433–437.

[15] A. Crosky, P. G. McDougall, and J. S. Bowles, *Acta Metall.*, 1980, vol. 28, pp. 1495–1504.

[16] C. P. Luo and G. C. Weatherly, *Acta Metall.*, 1987, vol. 35, pp. 1963–1972.

[17] C. P. Luo and G. C. Weatherly, *Phil. Mag. A*, 1988, vol. 58, pp. 445–462.

[18] K. R. Kinsman, E. Eichen, and H. I. Aaronson, *Metall. Trans.*, 1975, vol. 6A, pp. 303–317.

[19] E. Eichen, H. I. Aaronson, G. M. Pound, and R. K. Trivedi, *Acta Metall.*, 1964, vol. 12, pp. 1298–1301.

[20] R. F. Hehemann, K. R. Kinsman, and H. I. Aaronson, *Metall. Trans.*, 1972, vol. 3, pp. 1077–1094.

[21] C. Laird and H. I. Aaronson, *Acta Metall.*, 1969, vol. 17, pp. 505–519.

[22] G. Chen, J. K. Chen, J. K. Lee, and W. T. Reynolds Jr, Submitted to *Metall. Materi. Trans.*, in presss, 1994.

[23] A. G. Khachaturyan, *Theory of Structural Transformations in Solids*, John Wiley & Sons, New York, 1983.

[24] C. Laird and H. I. Aaronson, *Acta Metall.*, 1967, vol. 15, pp. 73–103.

[25] J. M. Howe, H. I. Aaronson, and R. Gronsky, *Acta Metall.*, 1985, vol. 33, pp. 639–648.

[26] G. J. Shiflet, in *Phase Transformations '87*, G. W. Lorimer, ed., THE INSTITUTE OF METALS, London, 1988, pp. 438–450.

[27] G. R. Purdy, *Scr. Metall.*, 1987, vol. 21, pp. 1035–1038.

[28] M. Enomoto, *Metall. Trans. A*, 1991, vol. 22A, pp. 1235–1245.

[29] H. I. Aaronson, T. Furuhara, J. M. Rigsbee, W. T. Reynolds Jr., and J. M. Howe, *Metall. Trans.*, 1990, vol. 21A, pp. 2369–2409.

[30] H. I. Aaronson and C. Laird, *Trans. AIME*, 1968, vol. 242, pp. 1437–1448.

[31] C. Laird and R. Sankaran, *J. Microscopy*, 1979, vol. 116, pp. 123–140.

[32] R. M. Aikin Jr. and M. R. Plichta, *Acta Metall.*, 1990, vol. 38, pp. 77–93.

[33] V. Perovic, L. M. Brown, and G. R. Purdy, *Acta Metall.*, 1981, vol. 29, pp. 889–902.

[34] D. E. Stephens, Y. J. M. Brechet, and G. R. Purdy, *Scr. Metall.*, 1988, vol. 22, pp. 1897–1902.

[35] J. D. Eshelby, *Proc. Roy. Soc.*, 1957, vol. A241, pp. 376–394.

[36] J. K. Lee, *Metall. Trans.*, 1991, vol. 22A, pp. 1197–1209.

[37] J. K. Lee and W. C. Johnson, *Scr. Metall.*, 1977, vol. 11, pp. 477–484.

[38] J. D. Eshelby, *Prog. Sol. Mech.*, 1961, vol. 2, pp. 89–103.

[39] C. P. Luo, *An Electron Microscope Study of the Crystallography and Interfacial Structures in A Ni-45Cr Alloy*, PhD thesis, The University of Toronto, 1986.

[40] D. P. Dandekar and A. G. Martin, *J. Mat. Sci. Letters*, 1989, vol. 8, pp. 1172–1173.

[41] T. Mura, *Micromechanics of Defects in Solids*, Martinus Nijhoff Publishers, Dordrecht, Netherlands, 1987.

[42] M. Hillert, *Lectures on the Theory of Phase Transformations*, TMS-AIME, New York, 1975.

[43] P. Nash, *Bulletin of Alloy Phase Diagrams*, volume 7, 1986.

[44] B. W. Leitch and M. P. Puls, *Metall. Trans. A*, 1992, vol. 23A, pp. 797–806.

[45] G. C. Weatherly and R. B. Nicholson, *Phil. Mag.*, 1968, vol. A 17, pp. 801–831.

[46] B. J. Kestel, *Ultramicroscopy*, 1984, vol. 19, pp. 213–216.

[47] H. Gleiter, *Acta Metall.*, 1969, vol. 17, pp. 565–572.

[48] R. W. Fonda, W. A. Cassada, and G. J. Shiflet, *Acta Metall. Mater.*, 1992, vol. 40, pp. 2539–2546.

[49] J. K. Chen and W. T. Reynolds Jr., Unpublished work, Virginia Polytechnic Institute and State University, 1993.

[50] V. Perovic and G. R. Purdy, *Scr. Metall.*, 1983, vol. 17, pp. 1305–1309.

[51] C. Atkinson, *Proc. Roy. Soc.*, 1982, vol. A384, pp. 107–133.

[52] V. Perovic, L. M. Brown, and G. R. Purdy, *Acta Metall.*, 1979, vol. 27, pp. 1075–1084.

[53] C. Laird and H. I. Aaronson, *J. Inst. Metals*, 1968, vol. 96, pp. 222–223.

[54] T. Furuhara, J. M. Howe, and H. I. Aaronson, *Acta Metall. Mater.*, 1991, vol. 39, pp. 2873–2886.

[55] C. Atkinson, K. R. Kinsman, and H. I. Aaronson, *Scr. Metall.*, 1973, vol. 7, pp. 1105.

[56] R. Sankaran and C. Laird, *Acta Metall.*, 1974, vol. 22, pp. 957.

[57] C. A. Dubé, PhD thesis, Carnegie Institute of Technology, 1948.

[58] R. F. Mehl and C. A. Dubé, *Phase Transformations in Solids*, John Wiley, New York, 1951.

[59] J. Ruzickova and B. Million, *Materials Sci. Eng.*, 1981, vol. 50, pp. 59–64.

[60] E. S. K. Menon, R. W. Hyland, and H. I. Aaronson, *Scr. Metall.*, 1984, vol. 18, pp. 367–370.

[61] G. J. Jones and R. K. Trivedi, *J. App. Phys.*, 1971, vol. 42, pp. 4299–4304.

[62] C. Atkinson, *Proc. Roy. Soc.*, 1981, vol. A378, pp. 351–368.

[63] C. Zener, *Trans. AIME*, 1946, vol. 167, pp. 550–595.

[64] J. W. Christian and D. V. Edmonds, in *Proceedings of an International Conference on Phase Transformations in Ferrous Alloys*, A. R. Marder and J. I. Goldstein, eds., TMS-AIME, Warrendale, PA, 1984, pp. 307–312.

[65] F. J. J. van Loo, B. Pieraggi, and R. A. Rapp, *Acta Metall.*, 1990, vol. 38, pp. 1769–1779.

[66] B. Pieraggi, R. A. Rapp, F. J. J. van Loo, and J. P. Hirth, *Acta Metall.*, 1990, vol. 38, pp. 1781–1788.

[67] J. M. Howe, T. Abinandanan, C. S. Chiang, T. Furuhara, N. Prabhu, and H. I. Aaronson, *Scr. Metall.*, 1987, vol. 21, pp. 1639–1643.

[68] H. I. Aaronson, J. M. Rigsbee, T. Furuhara, N. Prabhu, W. T. Reynolds Jr., and J. M. Howe, *Scr. Metall.*, 1989, vol. 23, pp. 279–284.

[69] A. Eikum and G. Thomas, *Acta Metall.*, 1964, vol. 12, pp. 537–545.

[70] R. Sankaran and C. Laird, *Phil. Mag*, 1974, vol. 29, pp. 179.

[71] J. M. Rigsbee and H. I. Aaronson, *Acta Metall.*, 1979, vol. 27, pp. 365.

[72] G. J. Shiflet, Unpublished work, University of Virginia, 1994.

[73] J. K. Chen, G. Chen, and W. T. Reynolds Jr., Unpublished work, Virginia Polytechnic Institute and State University, 1994.

[74] E. C. Bain and N. Y. Dunkirk, *Trans. AIME*, 1924, vol. 70, pp. 25–46.

[75] C. M. Wayman, *Introduction to the Crystallography of Martensitic Transformations*, Macmillan Series in Materials Science, Macmillan, NY, 1964.

[76] J. F. Nye, *Physical Properties of Crystals*, Oxford University Press, London, 1957.

Appendix A

Determination of the Transformation Strain Tensor and the Invariant Line Vector in the System Studied

The invariant line is calculated from the Bain strain and a lattice rotation relating the fcc and bcc phases. The Bain strain, **B**, generates a bcc lattice from the fcc lattice[74, 75]. This strain produces the Bain lattice correspondence of $[110]_{fcc}$ // $[010]_{bcc}$, $[1\bar{1}\,0]_{fcc}$ // $[100]_{bcc}$ and $[001]_{fcc}$ // $[001]_{bcc}$. An additional rigid body rotation, **R**, is applied to produce the Kurdjumov-Sachs orientation relationship. Thus, a vector in the bcc phase (expressed in the fcc coordinate system) can be written:

$$\mathbf{X_b} = \mathbf{RB}\,\mathbf{X_f} \tag{A.1}$$

The IL is defined as a vector which is neither distorted nor rotated[10]after transformation. Mathematically,

$$\mathbf{X_b} = \mathbf{X_f} \equiv \mathbf{X}_{\mathrm{IL}} \tag{A.2}$$

Substituting Equation A.2 into A.1, the condition for the invariant line is derived.

$$(\mathbf{RB} - \mathbf{I})\,\mathbf{X}_{\mathrm{IL}} = \mathbf{0} \tag{A.3}$$

Equation A.3 is satisfied only if the determinant of $\mathbf{RB} - \mathbf{I}$ is zero. Following Luo and Weatherly[16], the Kurdjumov-Sachs orientation relationship is employed. Therotation matrix, **R**, is then[75]:

$$\mathbf{R} = \begin{pmatrix} 0.9838773 & 0.0648404 & 0.1666763 \\ -0.0529177 & 0.9957778 & -0.0750079 \\ -0.1708362 & 0.0649785 & 0.9831545 \end{pmatrix} \tag{A.4}$$

and the Bain strain, **B**, is given by:

$$\mathbf{B} = \begin{pmatrix} \frac{\sqrt{2}}{\left(\frac{a_f}{a_b}\right)} & 0 & 0 \\ 0 & \frac{\sqrt{2}}{\left(\frac{a_f}{a_b}\right)} & 0 \\ 0 & 0 & \frac{1}{\left(\frac{a_f}{a_b}\right)} \end{pmatrix} \tag{A.5}$$

Using a lattice parameter ratio, $a_{fcc}/a_{bcc} = 1.25532$ [16], and a coordinate system defined by the fcc axes [100], [010] and [001], the quantity **RB - I** becomes:

$$\mathbf{RB} - \mathbf{I} \equiv u_{i,j}^T = \begin{pmatrix} 0.1086945 & 0.0731089 & 0.1328213 \\ -0.0596932 & 0.1221102 & -0.0596932 \\ -0.1924953 & 0.0731089 & -0.2166030 \end{pmatrix} \tag{A.6}$$

This quantity describes the displacements the material undergoes during transformation. We refer to it loosely as the displacement tensor and denote it as $u_{i,j}^T$. To obtain the stress-free transformation strain used in the strain energy calculations (Equation 2.8), $u_{i,j}^T$ is expressed in the coordinate system of Figure 2.1b by applying an appropriate similarity transformation

$$u_{i,j}^T = \begin{pmatrix} -0.0305166 & 0.0003087 & -0.2105250 \\ -0.2649880 & 0.0000182 & -0.1695470 \\ -0.0059809 & 0.0007064 & 0.0446893 \end{pmatrix} \tag{A.7}$$

and the symmetric portion of $u_{i,j}^T$ is extracted[76]:

$$e_{ij}^T = \frac{1}{2}(u_{i,j}^T + u_{j,i}^T) = \begin{pmatrix} -0.0305166 & -0.1323397 & -0.1082530 \\ -0.1323397 & 0.0000182 & -0.0844203 \\ -0.1082530 & -0.0844203 & 0.0446893 \end{pmatrix} \tag{A.8}$$

The determinant of $\mathbf{RB} - \mathbf{I}$ is 0.0000397, a small but nonzero quantity. Consequently, a precise invariant line does not exist for this ratio of lattice parameters when the orientation relationship is assumed to be exactly Kurdjumov-Sachs. The only lattice parameter ratios that yield a zero determinant of $\mathbf{RB} - \mathbf{I}$ and thus have an exact IL for the Kurdjumov-Sachs orientation relationship are 1.225 and 1.333.

Although there is no exact IL for this alloy system for a KS orientation relation, the small value of the determinant suggests that there is an *approximately* invariant line. This can be shown using the continuum analogy employed by Wayman[75]. The operation of the Bain strain on the fcc phase can be represented by the distortion of a sphere by the Bain deformation. An undistorted cone of vectors in the deformed sphere (an ellipsoid) can be brought into coincidence with the original sphere by a rotation, Figure A. The IL is obtained by rotating the final cone such that it intersects the initial cone along a single line.

A nonzero determinant of **RB-I** implies the cones are over-rotated yielding two intersections rather than one. These intersections are undistorted, but slightly rotated by the transformation so they are not quite invariant. In the present work, an approximate invariant line was derived by selecting an intersection of the undistorted cones and imposing the restriction that the IL lie in the precipitate habit plane, $(1\ \bar{2}\ 1)_{fcc}$. This approach yields an approximate IL in the Ni–Cr system of $[\overline{1.16045}\ \overline{0.080225}\ 1]_{fcc}$. Luo and Weatherly[16] employed a different method to obtain an approximate IL that is close to this one, but lies slightly out of the $(1\ \bar{2}\ 1)_{fcc}$ habit plane of the precipitate.

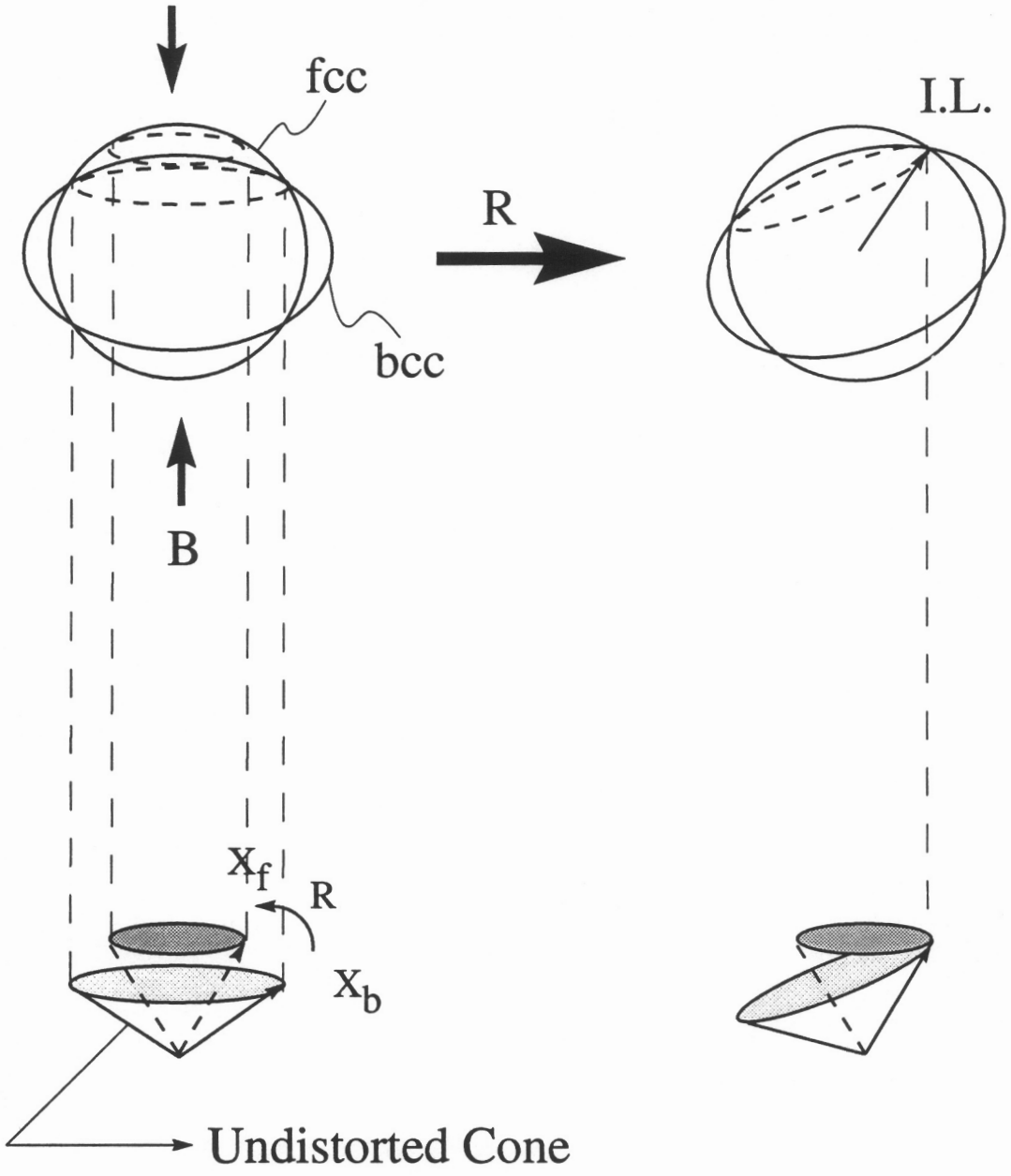

Figure A.1: Schematic representation of the Bain strain and the IL.

VITA

Mr. Gang Chen was born in October 1947 in Wuxi, Jiangsu, China. He graduated from high school in 1966, then went to the countryside as a farmer for three years and as a porter in Baoji railroad station for seven years during the Cultural Revolution. At age 31 in 1978 he had entered the Mechanical Engineering Department of Xi'an Jiaotong University. After graduation he worked as an assistant professor, lecturer in the Materials Engineering Department of Southwest Jiaotong University. In 1988 he joined Prof. H. I. Aaronson's research group at Carnegie Mellon University as a visiting scholar. In 1989 he came to Virginia Polytechnic Institute and State University to pursue a Ph.D. in Materials Science and Engineering on the role of interfacial structure in the evolution of precipitate morphology.

Gang Chen

陳剛

May 13, 1994